Dynamics of Melt-mediated Crystallization of Amorphous Silicon Films

Qiongying Hu

Submitted in partial fulfilment of the

requirements for the degree

of Doctor of Philosophy

in the Graduate School of Arts and Sciences

COLUMBIA UNIVERSITY

2011

ABSTRACT

Dynamics of Melt-mediated Crystallization of Amorphous Silicon Films

Qiongying Hu

This thesis reports on the new experimental findings and the corresponding conclusions that were made regarding the pulsed-laser-induced melting-and-solidification behavior of a-Si films. In particular, it focuses on investigating the melt-mediated crystallization details that are associated with the a-Si films, which presumably do not contain preexisting microcrystal clusters (as for instance can be formed via high-dose ion-irradiation of Si wafers and PECVD deposition of a-Si films). Whereas the behavior of microcrystalline-cluster-containing a-Si films within the partial-melting regime was well characterized and accounted for [1], a more intrinsic, and, therefore, more fundamentally important situation involving microcrystalline-cluster-deficient a-Si films in the partial melting regime has yet to be definitively resolved. The present thesis addresses this unsatisfactory situation.

The samples used in this work consisted of 50nm to 200nm dehydrogenated PECVD a-Si films (with or without additional ion irradiation of the films) on SiO_2-coated glass and quartz substrate. Single-shot irradiation experiments

using an excimer-laser-based system were conducted at various pulse durations (30ns-Gaussian-profile beam to 250ns beam obtained via an optical pulse duration extender) and at various energy densities. Extensive *in situ* transformation analysis was performed using both front-side and back-side transient reflectance measurements also microstructural characterization of the irradiated films was conducted using TEM and AFM.

The experimental findings obtained in this investigation reveal that these a-Si films can melt and solidify in ways that are quite distinct, more varied, and highly complex compared to those encountered in microcrystalline-cluster-rich a-Si films. Specifically: (1) spatially dispersed and temporally stochastic nucleation of crystalline solids occurring relatively effectively at the moving liquid-amorphous interface, (2) very defective crystal growth that leads to the formation of fine-grained Si proceeding, at least initially after the nucleation, at a sufficiently rapidly moving crystal solidification front, and (3) the propensity for local preferential re-melting of the defective regions and grain boundaries (while the beam is still on) are some of the fundamental factors that can participate and affect how these films melt and solidify. We discuss, by providing an extensive and critical review of the relevant papers, how the present conclusions are fundamentally distinct from those that have been made by the previous investigators in the field. The implications of these findings on the conventional ELA (i.e., excimer-laser annealing) method as well as the possibility of developing

partial-melting-regime-based ultra-high-throughput crystallization methods are also discussed.

Table of Contents

List of Figures

Dedication

This thesis is dedicated to my parents. Their support and encouragement of me to go after my goals in life have been my constant inspiration.

Acknowledgements

I would like to express my sincere thanks to the following people:

Professor James S. Im, my thesis advisor, without whom this thesis would not have taken shape. I attribute this work to his patient guidance and generous support. His scientific excellence and enthusiasm for research has always been a model for me. I feel grateful to have done my thesis work under his supervision; there is an old Chinese saying that may best describe my feelings over these years: "A teacher for a day is a father for a lifetime."

All the fantastic members in RRG, past and present, who have provided tremendous help over the past few years. Dr. Yikang Deng, who initially set up the TR measurement system and helped me with many difficult experiments; Dr. Alexander Limanov, Dr. Ui-Jin Chung and Adrian Chitu, who trained me in the use of different microscopes and provided invaluable technical suggestions; Dr. Paul van der Wilt, Monica Chahal, Gabriel Ganot and Wesley Hattan, who offered me unlimited help and guided me through some particularly tough times; Min Hwan Choi, a wonderful friend who was always willing to help me in any way; and Ting Li, who helped take some AFM images, used in this thesis, during the final busy months.

I would also like to acknowledge Professor Michael O. Thompson of Cornell University, who generously accommodated us in his lab. More importantly, the results we obtained in Cornell helped solve many of the puzzles we encountered and constitute a very important part of this thesis.

Chapter 1 Introduction

1.1 Introduction

This thesis investigates the rapid phase transformation details associated with pulsed-laser induced melting and solidification of a-Si films.

Fundamentally, melting of a-Si corresponds to the simplest example of phase transitions between two metastable phases in condensed systems; as a-Si can be identified as an elemental metastable solid phase (distinct from configurationally frozen liquids). The melting of a metastable solid phase inevitably requires rapid heating and melting, since slow heating of the material would kinetically likely lead to solid-phase transformation of the metastable solid phase into a thermodynamically more stable solid phase. As pulsed-laser irradiation can induce rapid melting and solidification of various metallic and semiconducting materials, it represents an appropriate experimental tool by which various fundamental aspects of far-from-equilibrium melt-mediated transitions of semiconductor and other materials systems can be studied.

Previous studies involving the pulsed-laser-induced melting of a-Si have demonstrated that a variety of solidification microstructures can be obtained when the beam provides sufficient energy to only "partially" melt a-Si. This indicates that the details and extent of melting can profoundly affect the microstructure of the resulting material. Even though this topic has been actively investigated over a number of years (since the early eighties), a number of important issues and details have not been resolved. (An overview of the experimental and theoretical studies conducted by previous investigators regarding pulsed-laser induced transformations of a-Si will be given in Chapter 2.)

Technologically, the understanding of pulsed-laser-induced melting and solidification of amorphous silicon films is ever-so-relevant in that the use of the method (in the form of excimer-laser-induced crystallization) is presently being used for fabricating thin-film transistors (TFT) utilized in manufacturing advanced flat-panel displays (i.e., active-matrix liquid-crystal displays and active-matrix organic light-emitting diodes) [6]. As it is generally the case, the performance of these electronic devices can depend heavily on the microstructural quality of the solidified films. The present efficiency of the method can be identified as being less-than-satisfactory (in that approximately twenty-shots are required in the conventional "excimer-laser annealing" method). Therefore, we argue

that it is important to properly understand the details associated with melting and solidification of a-Si films, so that we can eventually design and develop laser-crystallization approaches to provide the desired and optimized polycrystalline Si films (i.e., uniform and low-defect-density materials) in a more efficient (i.e., high-throughput) manner.

In short, this thesis was motivated by (1) the aforementioned fundamental opportunity to identify/understand the transformation details pertaining to melt-mediated transitions involving partially melted a-Si films, and (2) the technological opportunity for developing, based on such fundamental details, better melt-mediated crystallization techniques for efficiently and effectively realizing high-performance TFTs.

1.2 Organization of Thesis

The rest of this thesis is organised as follows:

Chapter 2 discusses the background of the research topic presented in this thesis. The chapter includes a brief description of the phase-transformation-related fundamentals, and an overview of the relevant investigations that were previously conducted.

Chapter 3 describes the procedural details of the thesis consisting mostly of the experimental aspect of the present work (i.e., sample configuration, experimental setup, and sample characterization methods), as well as the numerical simulation program also employed in this thesis.

Chapter 4 corresponds to the most significant chapter of the present thesis in that it presents the main experimental results regarding excimer-laser induced melting and solidification of dehydrogenated PECVD a-Si films using a "short duration" pulse with Gaussian-temporal profile. Based on the microstructure and *in-situ* reflectance based results, we suggest a working model in which (1) the heterogeneous nucleation of crystal Si at the melting interface (i.e., moving interface between liquid and amorphous Si) is the solidification initiation/triggering mechanism, (2) subsequent post-nucleation solidification proceeding defectively (i.e., crystal growth in the defective mode of growth), and (3) spatially localized preferential re-melting, surprisingly, while the beam is still on can all be important in determining the final microstructure of the solidified films. We also show how our model, which we argue is the only model that consistently accounts for what we (and others) have previously observed to date, is fundamentally different from those that were previously suggested and argued by other investigators.

Based on the model we formulate in Chapter 4, the experimental results obtained upon laser irradiation of a-Si films with a "double-peak" pulse temporal profile (Chapter 5) and "long pulse duration" profile (Chapter 6) are analyzed. These experimental results, which show clearly distinct trends and features, are argued as actually being consistent and supportive of the proposed model. The implications of these findings are also discussed in the chapter; including a suggestion for a new ultra-high-throughput laser crystallization method.

Chapter 7 applies the one-dimensional numerical simulation to quantitatively and indirectly analyze the situation involving idealized melting and solidification of amorphous Si (without crystal Si nucleation).

The simulation analysis implies that the simple form of classical nucleation theory that treats heterogeneous nucleation by assuming constant contact angle at the planar interface may not be applicable to the present situation.

Chapter 8 summarizes the findings of this work and provides suggestions for possible future research.

Chapter 2 Background

2.1 Properties of Amorphous Silicon

Three distinct condensed phases of Si -- crystalline, amorphous and liquid -- have been identified as existing under one atmosphere pressure [7].

A schematic diagram illustrating the relative Gibbs free energies of the liquid, crystalline and amorphous phases of Si is shown in Figure 2.1. This figure provides the thermodynamic basis for identifying the various possible phase transformations that can occur in Si. As indicated in Figure. 2.1, a-Si is a metastable phase with respect to c-Si below a "virtual" coexistence temperature (about 2300 K). Also it is well established that a-Si can melt by a first order transition, provided that heating is carried out sufficiently rapidly that the extent to which solid-phase crystallization takes place is negligible during the heating period [8]. (This kinetically and procedurally requires heating on the sub-microsecond time scale.)

a-Si is viewed as a distinct metastable solid phase with a melting point about 200 K lower than that of c-Si. Therefore, the transition of a-Si to l-Si is assumed to be first order and discontinuous [9]. This behavior of a-Si is distinct from that of many other amorphous materials that show a continuous transition to the liquid phase upon heating (i.e., "glasses" that are viewed as configurationally frozen liquids). The concept of non-glassy amorphous Si was first formulated by Turnbull and Spaepen [10] and Chen and Bagley [11] in 1978, and confirmed by later experimental results [12, 13].

Structurally a-Si is a four-fold coordinated covalently bonded solid that lacks long range order. This can be ideally described in a simplified manner by a continuous random network (CRN) model [14]. Moreover, due to the disordered nature of the material some atoms have dangling bonds. Physically, these dangling bonds represent defects in the continuous random network and may cause anomalous electrical behavior. Direct use of amorphous Si for electronic devices, therefore, usually requires the passivation of these dangling bonds by effectively incorporating hydrogen atoms; hydrogenated a-Si can be obtained via plasma-enhanced chemical vapor deposition (PECVD) processes [15].

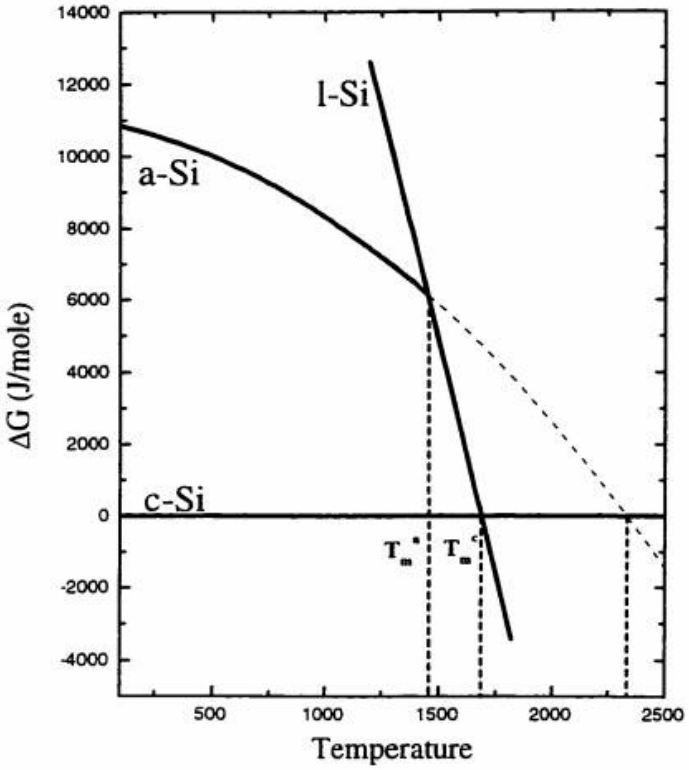

Figure 2.1 The isobaric Gibbs free energy of liquid and amorphous phase of silicon, relative to c-Si. [16]

2.2 Phase Transformation Fundamentals

Nucleation and growth are two fundamental components in a first-order phase transformation. In this section, we will briefly review the theoretical background and review some of the key formulas of each component.

2.2.1 Classical Nucleation Theory

Nucleation is a process in which a new phase appears within the less thermodynamically stable parent phase. Classical nucleation theory (CNT) is a model that takes into account the thermodynamic and kinetic aspects of the phenomenon [17]. It explains nucleation by considering the potential energy barrier associated with the creation of solid nuclei. The total change in free energy associated with the formation of a small cluster is expressed as a sum of two terms: one resulting from the volumetric-free-energy consideration and another resulting from the interfacial-energy considerations. The change in the sum of these two terms as a function of the cluster size determines whether a given small cluster is likely to grow (when supercritical) or shrink (when subcritical).

$$\Delta G_f = V_S\left(G_S^{vol} - G_L^{vol}\right) + A_{SL}\gamma_{SL}, \tag{2.1}$$

where V_S and A_{SL} are the volume and the interfacial area of the cluster, G_S^{vol} and G_L^{vol} are the free energies per unit volume of the solid and the liquid phase respectively, γ_{SL} is the interfacial tension (i.e., the excess free energy per unit area of the solid/liquid interface), and ΔG^{vol} as shown in equation (2.2), is smaller than zero.

$$G_S^{vol} - G_L^{vol} = \Delta G^{vol} < 0. \tag{2.2}$$

From the above equation it can be seen that the disappearance or appearance of a stable nucleus depends on the free energy of the system. As shown in Figure 2.2, when the radius of a spherical nucleus is smaller than the critical size, a nucleus will tend to shrink and eventually disappear. On the other hand, when it is larger than the critical size, a nucleus will tend to grow.

The maximum value of ΔG_f which corresponds to the critical cluster size can be obtained by setting $\partial \Delta G_f / \partial r = 0$. This gives the critical size as:

$$r^* = -\frac{2\gamma_{SL}}{\Delta G^{vol}}, \tag{2.3}$$

and the free energy at the critical cluster size is:

$$\Delta G^*_f = \frac{16}{3}\pi \frac{\gamma_{SL}^3}{\left(\Delta G^{vol}\right)^2}. \tag{2.4}$$

From the statistical mechanical models such as Volmer-Weber and the Becker-Doring models, it can be derived that the population of supercritical clusters per unit volume obeys a Boltzmann distribution. Since nucleation is defined as the appearance of supercritical clusters, the nucleation rate can be approximated by the number of critical clusters per volume, P(r*), multiplied by the rate of attachment of additional monomers onto the nuclei, I_0. The resulting steady state homogeneous nucleation rate is written as:

$$I_{\text{hom}}^{ss}(T) = I_0(T)\exp\left(\frac{-\Delta G_f^*}{kT}\right), \tag{2.5}$$

where I_0 is the kinetic prefactor.

For heterogeneous nucleation, the case where nucleation occurs preferentially at preexisting interfaces, the nucleation rate can be formulated as:

$$I_{het}^{ss}(T) = I_{0,het}(T)\exp\left(\frac{-\Delta G_f^* f(\theta)}{kT}\right). \tag{2.6}$$

Where f(θ) is a function of contact angle θ that depends on the interfacial energies of the three interfaces (Figure 2.3). The contact angle can be calculated from a force balance on a solid embryo in contact with a wall in a liquid matrix as follows:

$$\gamma_{LW} = \gamma_{LS}\cos\theta_c + \gamma_{WS} \ . \tag{2.7}$$

Figure 2.4 shows a schematic of nucleation rate as a function of temperature. Note that the Y axis represents the logarithm of the nucleation rate; the nucleation rate is so sensitive to the temperature that, for a given quench rate, a unique nucleation temperature can be effectively specified.

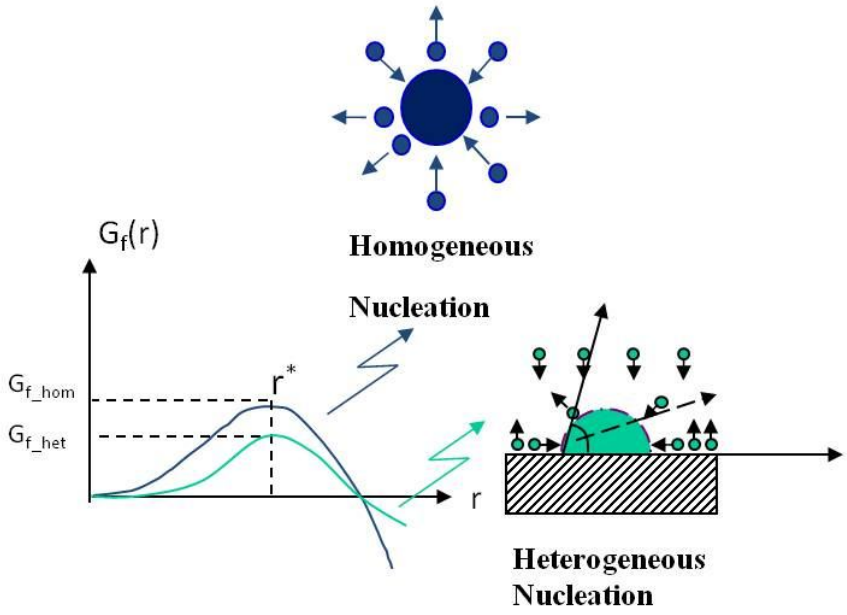

Figure 2.2 Homogeneous vs. heterogeneous nucleation. Homogeneous nucleation occurs when a solid spherical cluster present within a supercooled liquid media reaches the critical size (r*) of nucleation. Heterogeneous nucleation forms on pre-existing surfaces that reduce the free energy barrier to reach the critical radius, r*. [18]

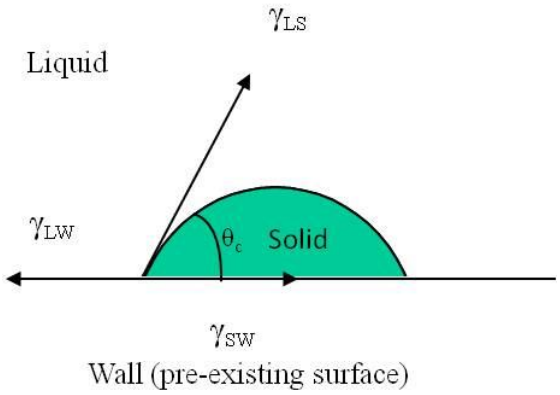

Figure 2.3 The formation of a nucleus on a flat heterogeneity.

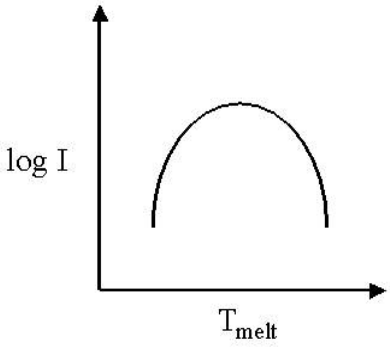

Figure 2.4 Schematic of nucleaiton rate vs temperature.

2.2.2 The Interface Response Function

The rate at which liquid-solid interface moves during melting and solidification of an elemental system is determined by the departure of the interface temperature with respect to the equilibrium melting point between the two phases. This kinetic relationship is refereed as interface response function (IRF), and constitutes an important relationship in the study of melting and solidification under far-from-equilibrium conditions. It describes the movement of the interface in response to the interface temperature that is either undercooled (when solidifying) or superheated (when melting) relative to the melting point.

Based on the continuous growth model that assumed an even distribution of sites over the interface onto which attachment of atoms may occur, a general description of the temperature-dependent interfacial velocity of an elemental system can be given as [10, 19, 20]:

$$V(T) = v_0(T)\left[1 - \exp\left(-\frac{\Delta G_{LS}}{RT}\right)\right], \tag{2.8}$$

where $v_0(T)$ is the intrinsically limited maximum forward velocity, ΔG_{LS} is the absolute value of the free energy of crystallization (free energy difference between liquid and solid), and $R=kN_A$. The term within the brackets stems from the temperature-dependent difference between the

forward and reverse rates of solidification. As shown in the above equation, V(T) is positive for solidification and negative for melting. The kinetic prefactor, $\nu_0(T)$, can be described as a function of interfacial rearrangement kinetics as shown as:

$$v_0(T) = fm_i d\left[1 - \exp\left(-\frac{\Delta G^*}{RT}\right)\right] \quad , \tag{2.9}$$

where f is the fraction of active sites at the interface, m_i is the jump frequency, d is the interface travel distance per successful jump, and ΔG^* is the free energy of activation.

At small deviations from the equilibrium melting temperature, ΔG_{LS} can be approximated as [20]:

$$\Delta G_{LS} \approx \left((T_m - T)/T_m\right)\Delta H \quad , \tag{2.10}$$

where T_m is the equilibrium melting temperature, and ΔH the enthalpy difference between the solid and liquid phases (i.e., latent heat of fusion).

The following equation can be derived, for small undercooling conditions, by substituting equation (2.10) into equation (2.8):

$$V(T) = K\left|T_m - T\right| \quad , \tag{2.11}$$

where K is the proportional constant. (The interface response function can be conveniently described in term of the above linear relationship for small-to-moderate deviations from T_m.)

The interface response functions of Si have been studied extensively by numerous investigators [21-23]. Figure 2.5 shows quantitative interface response functions Stolk *et al* [24] derived from experimental measurements analyzed using a thermal analysis based on equation (2.8).

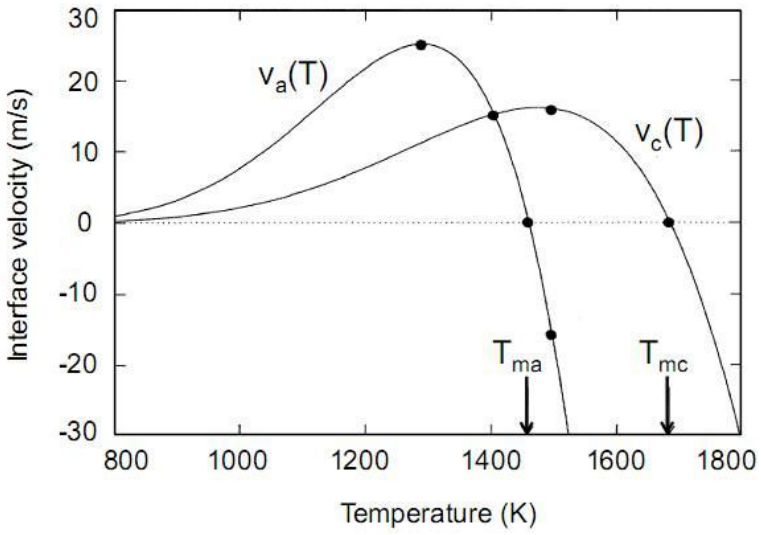

Figure 2.5 Interface response functions of c-Si and a-Si derived by Stolk and Polman [24]. The velocities of the interfaces are zero at the respective melting temperatures.

2.3 Laser Induced Melting and Solidification of Amorphous Silicon

2.3.1 Pulsed-laser Annealing (PLA) of Ion Implantation Amorphized Si Layer

One of the first exploitations of laser annealing was the removal of ion implantation-induced lattice damage at the surface of ion-doped Si wafers. Extensive studies performed during this period have yielded interesting experimental results and some critical concepts. One of these important conclusions is that a-Si can be directly melted (as opposed to undergoing continuous viscosity change) at a temperature, which is about 200 K below the melting point of c-Si [8, 25].

Studies on pulsed laser annealing of a-Si layer also show that when the incident laser energy density is sufficient to induce partial melting of a-Si layer, a phenomenon called explosive crystallization can be observed. This process was found to convert a-Si into fine-grained polycrystalline Si via a melt-meditated crystallization mechanism involving a buried liquid layer [26]. This buried liquid layer is at a temperature higher than the melting point of a-Si, while lower than the melting point of c-Si, and therefore can propagate into the a-Si matrix by simultaneously melting a-

Si and freezing the melted liquid layer into c-Si. Due to a latent heat difference between c-Si and a-Si, the propagation can be self-sustaining under appropriate thermal environments.

By using *in situ* transient reflectance and transient conductance measurements, Thompson *et al* [25] was able to identify and describe the overall sequence of events in melting and solidification of a-Si layers. Nevertheless, one could note that they did not address some key transformation–related issues. For instance: (1) how and where the c-Si phase is first nucleated (i.e., within the shallow pool of undercooled liquid Si in contact with a-Si), and (2) the details of explosive crystallization (i.e., how it is propagated) that leads to the formation of the fine-grained microstructure [27].

Tsao and Peercy [28] and Roorda and Sinke [29] have proposed models to address the above questions concerning the initial formation and subsequent propagation of the buried melt layer. A detailed description as well as full discussion of these models will be presented later in Section 4.3.1 and 4.4.2.

2.3.2 Excimer-laser Crystallization (ELC) of Thin Si Films on SiO_2

Excimer-laser crystallization of a-Si is a glass-substrates-compatible method that converts initially amorphous Si films into device-worthy crystalline Si films [30]. This method can accomplish this as a result of the capability of an excimer laser to impart a short-duration high-energy pulse at a UV wavelength, which is well coupled to Si, and the small thermal mass of Si films.

The samples for ELC are a-Si films on glass substrates formed by a deposition process on SiO_2–coated glass substrates. The most commonly used deposition methods include low temperature chemical vapor deposition (LPCVD) and plasma enhanced chemical vapor deposition (PECVD). Of these, PECVD can be further identified as the method which is utilized nearly exclusively in mass production.

2.3.2.1 Characterization of ELC: Different Melting Regimes

In general, irradiating a-Si or c-Si films on SiO_2 using a short-duration laser pulse can lead to several distinct melting and solidification scenarios. It has been identified by Im *et al* [1, 31] that excimer laser irradiation of thin films can be characterized in terms of two major regimes (i.e., low-energy-density/partial-melting and high-energy-

density/complete-melting regimes) and a sub-regime (near-complete-melting/super-lateral-growth regime).

Figure 2.6 illustrates a simple example of melting c-Si films under different energy densities.

(1) In the partial melting regime, the irradiated energy density is above the surface melting threshold to induce primary melting but not sufficiently high enough to melt through the film entire thickness. Si films are partially melted and primarily vertically re-growth proceeds from the un-melted under-layer.

(2) In the complete melting regime, the incident energy density is sufficiently high to fully melt the films. The transformation occurs via nucleation and growth of solids in a rapidly quenched and deeply supercooled liquid.

(3) The near-complete-melting sub-regime is encountered when the energy density range falls between the above two regimes. Large grains are formed, resulting from the lateral growth of isolated un-melted solids at the bottom interface.

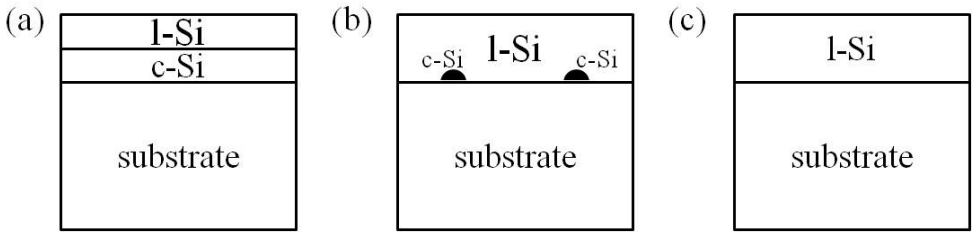

Figure 2.6 Schematic diagrams showing different melting regimes for excimer laser irradiation of Si films: (a) partial melting regime, (b) super lateral growth (SLG) sub-regime and (c) complete melting regime. The starting material is assumed to be c-Si for simplicity.

2.3.2.2 Partial Melting of as-deposited LPCVD a-Si Films

As-deposited LPCVD a-Si films are known to contain a considerable number of microcrystalline Si clusters. Yoon *et al* [16, 32] reported that the overall melting behavior of as-deposited LPCVD films can be satisfactorily explained using the microcrystalline model (in which the embedded micro-crystals are identified as the key solidification initiating agents). According to this model: (1) a thin amorphous surface layer (~ 10nm) directly undergoes melting, (2) the molten surface layer is then rapidly solidified as the preexisting microcrystalline Si clusters, which are supercritical with respect to the metastable l-Si surrounding the cluster grow, (3) the latent heat released from solidification generates a thin buried molten layer, which then propagates towards the substrate by the

melt-mediated explosive crystallization process, (4) the fine-grained surface region can, sequentially undergo re-melting while the buried layer propagation is occurring, and (5) the primary liquid melting front propagates towards the substrate until the maximum point of melting is achieved.

The signature oscillation in *in situ* transient reflectance measurements due to early and promptly triggered explosive crystallization and the resulting fine-grained polycrystalline Si microstructure is shown in Figure 2.7.

(a)

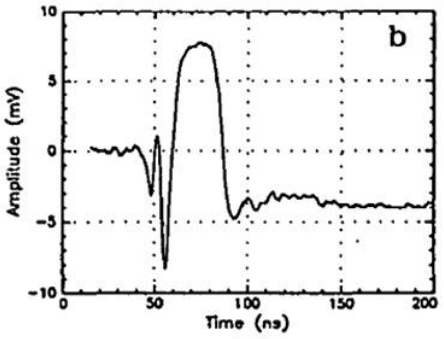

(b)

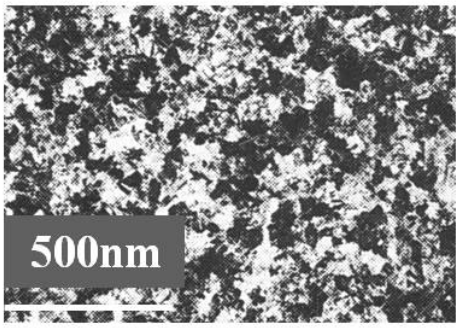

Figure 2.7 100nm LPCVD a-Si films irradiated with short pulse excimer laser: (a) a representative Front-side TR trace (b) Planar view TEM micrograph obtained by Im *et al* [1, 33].

Chapter 3 Experimental Approach and Analysis

3.1 Introduction

This chapter describes the details associated with the experimental procedures and techniques employed in this thesis for investigating the melt-mediated phase transitions manifested in excimer-laser irradiated PECVD a-Si films. In addition to addressing various elementary details associated with our irradiation experiments (i.e., sample configurations (Section 3.2), the irradiation system, and irradiation procedures, etc.), we elaborate on the two principle techniques (extensive microstructure characterization using TEM and AFM, and in-situ transformation analysis using front-side and back-side transient reflectance measurements) forming the basis from which our understanding is eventually developed (Section 3.3 and 3.4). Additionally, we describe a simple yet valuable numerical tool that will later be utilized to qualitatively evaluate and

quantitatively analyze the transformation-related details that are revealed in our experimental results.

3.2 Sample Configuration

The samples consisted of 50nm to 200nm a-Si films on SiO_2-coated glass and quartz substrates. Amorphous Si films were prepared by plasma-enhanced chemical vapour deposition (PECVD) and dehydrogenated at 500 ^{0}C. Before the actual a-Si deposition, a 300nm-thick buffer oxide layer was deposited on the glass substrates to ensure the cleanliness of the a-Si/oxide interface. A few dehydrogenated PECVD a-Si films were additionally self-ion irradiated with 100kev Si at the dose of $5x10^{15}$ ions/cm^2.

As discussed in more detail later, one important element of our experimental approach, which takes advantage of the transparent nature of glass and quartz substrates, consisted of *in-situ* back-side transient reflectance (BTR) analysis to probe the appearance and subsequent dynamics of the liquid region(s).

The samples we used were obtained from various industrial sources using state-of-the-art deposition chambers. In addition to qualifying our observations and conclusions as being directly applicable to real-

manufacturing processes, these device-grade quality samples permitted us to consistently study the intrinsic behavior of PECVD a-Si films. We have performed a number of experiments using various parameters and samples configurations; of these results, we have identified the set obtained from 100nm-thick dehydrogenated PECVD a-Si films on glass substrate as being the most meaningful and representative. These are presented in the following chapter.

3.3 Experimental Setup

The schematic diagram of our laser irradiation system is shown in Figure 3.1. The system consists of two major components: (1) an excimer laser and beam delivery optics and (2) *in situ* front-side and back-side transient reflectance (TR) measurement setup at two different wavelengths.

An excimer laser beam (308nm wavelength) with a pulse duration (ranging from ~30 to 250ns) is used in this thesis's experiments. It is important to note that the type of laser utilized corresponds to the very type of lasers that are pervasively employed in industrial laser-crystallization systems. After passing through a beam attenuator and splitter, the laser beam is shaped by a telescope lens, homogenized by a multi-lens homogenizer system, and expanded by a field lens. The beam

is then further shaped as it passes through the patterns on a Cr-on-quartz photo-mask, the image of which is then de-magnified (5X) and focused onto the sample surface through a projection lens. The sample stage is controlled by computer and can be translated in X, Y, and Z directions with 0.1 μm dynamic resolution. A calibrated energy meter receives a fraction of the original laser light from a beam splitter and monitors the laser pulse energy.

The probing laser beam, reflected off the front- and back-side of the sample, passes through focusing lenses and UV filters onto fast photo detectors (with less than 1ns rise time) before being recorded by a digital oscilloscope (Tektronix 3054C) with a maximum sampling rate of 5 Giga samples per second. The beam spot size at the sample surface for the probing diode lasers is approximately 100 μm in diameter.

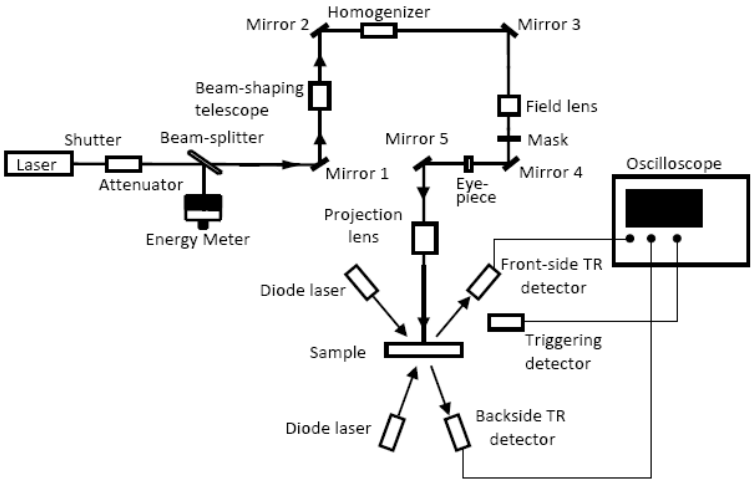

Figure 3.1 Schematic diagram of the laser irradiation system with *in situ* front-side and back-side transient reflectance measurement setup.

3.4 Microstructure Analysis

To characterize the microstructure of the irradiated films, planar TEM, cross-sectional TEM and AFM were used. The planar view TEM and cross-sectional TEM imaging work were performed on a JEOL JEM-100CX TEM at 100kev (Columbia University, New York, NY), and a JEOL JEM-2100F TEM at 200kev (KAIST, Daejeon, South Korea), respectively. AFM work was performed on a Digital Instruments AFM-4 in contact mode.

During the preparation of planar view TEM samples, secco-etchant [34] was used to strengthen the grain boundaries.

3.5 Numerical Modelling

Three dimensional numerical simulation (3DNS) [35, 36] is a powerful program designed primarily to treat melting and solidification problems encountered in the pulsed laser irradiation experiments. It uses a finite-difference model for heat flow and an interface-tracking model originating from the 1D simulation package by Thompson and Uttomark [37]. With later implementations introduced in two dimensional and three dimensional simulations [35, 36, 38], nucleation effects and structural changes could be modelled. We will briefly describe the key components in the algorithms used in this simulation package.

The finite difference scheme implemented in 3DNS subdivides the system into a 3D array of orthorhombic nodes as shown in Figure 3.2. The grid of nodes simultaneously models heat flow, interface motion and nucleation. By specifying each thermo-physical property in the form of temperature-dependant equations, we can numerically experiment with a thin film stack consisting of various materials, starting phases in each subregion.

Heat flow modelling is a critical component of 3DNS. The general continuity equations for temperatures are applied in each distinct region and across each interface. The general heat transport function is given as:

$$C_p(\phi,T)\frac{\partial T}{\partial t} = k_T(\phi,T)\nabla^2 T + \nabla k_T(\phi,T)\cdot\nabla T + \dot{q_L} + \dot{q_E} \quad . \tag{3.1}$$

Where C_p is the heat capacity, k_T is the thermal conductivity, $\dot{q_L}$ corresponds to latent heat release or consumption at an interface and $\dot{q_E}$ corresponds to heat generated by external sources as laser absorption.

The interface response function is a crucial component in 3DNS and is used to obtain local velocities at each times step. The function is based on the diffusion limited theory [20, 39] and is used in 3DNS as given below:

$$\left|v(T_i)\right| = an\cdot\exp\left(-\frac{DG_L^*}{k_B T}\right)\left(1-\exp\left(-\frac{\left|G_L - G_S\right|}{k_B T}\right)\right) \quad . \tag{3.2}$$

In the 3DNS package, a combined form of crystalline and amorphous interface response function can be used to express the extremely high cooling rate. The exact form can also be set by the users to simulate specific systems with different under cooling conditions.

Nucleation is a stochastic process [83], which involves a spontaneous appearance of solid nuclei in the melt when highly undercooled. Incorporating the stochastic nature of nucleation in undercooled liquid, the package utilizes the nucleation rate functions for steady state nucleation in undercooled liquid proposed by CNT [40] as shown below

for homogeneous and heterogeneous nucleation processes.

$$I_v(T) = I_{0v}(T)Exp\left[\frac{-\Delta G^*(T)}{k_b(T)}\right], \tag{3.3}$$

$$I_a(T) = I_{0a}(T)Exp\left[\frac{-\Delta G^*(T)f(\theta)}{k_bT}\right]. \tag{3.4}$$

The stochastic nature of nucleation is handled by the use of Poisson statistics where a nucleation event is viewed as a fluctuation in the parent liquid that successfully results in a critical size solid nucleus. Poisson statistics describes the probability of avoiding nucleation $P_{liq}(t)$ (zero successes) within time t for a given volume v_a kept under isothermal supercooled conditions as shown in equation below:

$$P_{liq} = \frac{(np)^0}{0!}e^{-np} = \exp\left[-\Gamma(T)\delta t\left(\frac{t}{\delta t}\right)\right] = \exp[-\Gamma(T)\cdot t], \tag{3.5}$$

where n is the number of independent trials in the nucleation process, p the probability of nucleation in each trial and $\Gamma(T)$ the nucleation frequency.

The probability for nucleation occurring within time t is given as follows:

$$P_{nuc} = 1 - P_{liq} = 1 - \exp[-\Gamma(T)t], \tag{3.6}$$

where P_{nuc} ranges from 0 to 1 and corresponds to the probability of nucleation occurrence in a node during a time step.

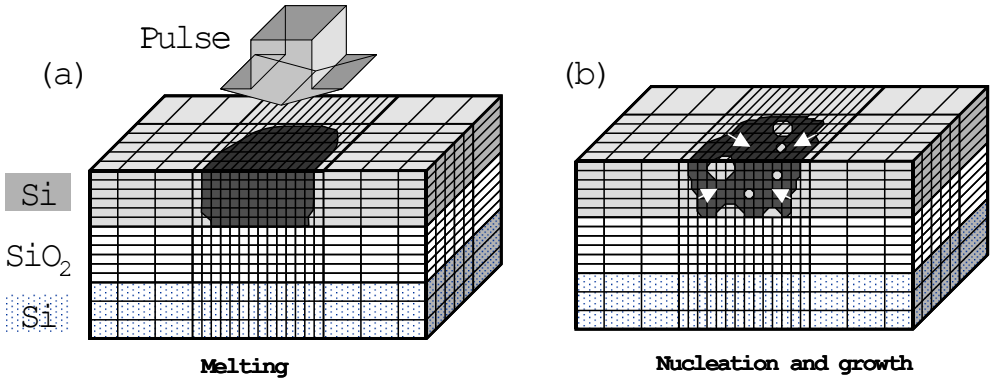

Figure 3.2 Schematic diagram [41] showing typical 3-dimensional node network used in 3DNS. Sample is subdivided into orthorhombic nodes of variable sizes. Laser pulse is incident on the top surface, here shown inducing melting of the top Si film in (a), followed by re-solidification and possible homogeneous or heterogeneous nucleation as shown in (b).

Chapter 4 Excimer Laser-induced Melting and Solidification of PECVD a-Si Films

4.1 Introduction

In general, irradiating amorphous or polycrystalline Si films on SiO_2 using a short-duration laser pulse can lead to several distinct melting and solidification scenarios. It is well established that the process can be characterized in terms of two major regimes (i.e., low-energy-density/partial-melting regime and high-energy-density/complete-melting regime) [1] and a sub-regime (i.e., near-complete-melting/super-lateral-growth regime) [31].

In this chapter, we focus our attention on investigating the details associated with melting and solidification of dehydrogenated PECVD a-Si films irradiated within the low-energy-density/partial-melting regime. Whereas the behavior of microcrystalline-cluster-containing LPCVD a-Si

films within the partial-melting regime was characterized and explained (in terms of the early and rapid microcrystal-triggered explosive crystallization of the films followed sequentially by uniform re-melting and vertical solidification of the crystallized layer [16, 32]), a more intrinsic and significant situation (scientifically and technologically) involving microcrystalline-cluster-deficient a-Si films (e.g., PECVD a-Si) in the partial melting regime has yet to be resolved. Addressing this unsatisfactory situation constitutes the main aim of this investigation.

Based on observations from both the microstructural and *in situ* time-resolved transient-reflectance analyses, we identify the melting and solidification sequences that are manifested in the process. We conclude that heterogeneous nucleation of c-Si occurring at the melting front (i.e., the moving l-Si/a-Si interface) is the key event that locally triggers and initiates a series of transient solidification and melting transitions (including the long-investigated, yet not fully resolved, topic of explosive crystallization). By providing an extensive and critical review of the relevant papers, we will discuss how the present conclusions are fundamentally distinct from those that have been made by previous investigators in the field.

4.2 Experimental Setup

Single shot irradiation experiments using a XeCl excimer-laser-based system (308nm wavelength) were conducted at various energy densities over the entire partial-melting window. The temporal profile of the irradiation laser pulse is shown in Figure 4.1, consisting essentially of simple Gaussian-like peak (and weak and insignificant residual fluctuations). This is an important experimental element to appreciate for a couple of reasons: (1) this approximately 30ns pulse duration is similar to those which have been used in previous investigations on partial-melting experiments [25, 42-46], permitting more direct comparisons to be made to a number of previously attained experimental results, and (2) such a simple temporal profile leads to simpler transformations and more rigorous interpretations, thereby permitting more definitive conclusions to be reached. As alluded to previously, *in situ* front-side and back-side transient reflectance measurements were carried out at 650 and 790nm, at an incident angle of 40^{o} and 20^{o}, respectively.

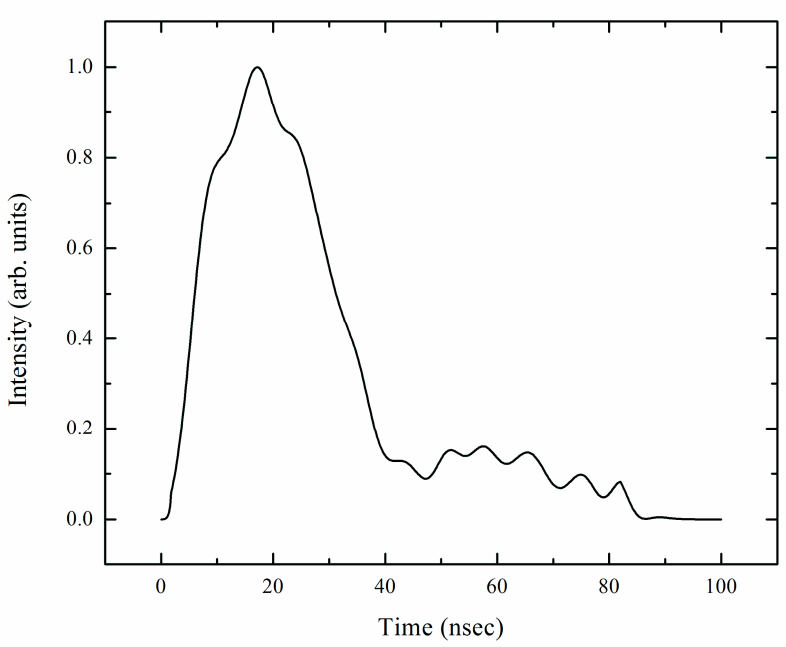

Figure 4.1 Temporal profile of irradiation laser pulse (308nm, FWHM ~30ns).

4.3 Experimental Results

The corresponding microstructures of Si films irradiated at energy densities over the partial melting regime were studied by means of detailed planar and cross-sectional TEM images, while surface morphology was measured by AFM in contact mode. This section presents, and builds arguments on the experimental results from both the microstructure and *in situ* transient reflectance analyses.

4.3.1 Microstructure Analysis

Figure 4.2 and 4.3 show a series of planar and cross-sectional TEM micrographs of 100nm dehydrogenated PECVD a-Si films, following single-shot irradiation at various energy densities all in the partial melting regime.

At low energy density just above the surface melting threshold, both planar (Figure 4.2 (a)) and cross-sectional (Figure 4.3 (a)) TEM micrographs indicate that the film is converted into a fine-grained (~10nm-sized) polycrystalline microstructure (fg-Si). Such a fg-Si microstructure has been previously observed in similar experiments with ion-implanted amorphized Si layer [25, 47, 48] and as-deposited amorphous films [49, 50] at low energy densities, and have been identified as being associated with the phenomenon of "melt-mediated" explosive crystallization. As was previously discussed in Section 2.3, explosive crystallization of a-Si is a process driven by the difference in the free energies of a-Si, l-Si, and c-Si between the a-Si and c-Si melting temperatures, and involves the rapid propagation of a thin buried molten layer [25, 51].

To account for the formation of fg-Si, previous investigators have suggested two copious-nucleation-based models (wherein a critical and incorrect assumption was made that each grain within the material

resulted from a single nucleation event). First, Tsao and Peery [28] have proposed that c-Si nuclei form continuously and at extremely high rates at the moving l-Si/a-Si melting interface and grow into the surrounding undercooled liquid. Additionally, Roorda and Sinke [29] have suggested that small crystallites nucleate homogeneously at extremely high rates within the a-Si matrix during the heating period and grow rapidly into the surrounding undercooled liquid Si as the crystal nuclei containing matrix melts. Once again, these two models both assume that copious and continuous nucleation of crystals takes place at rates that lead to the formation of fg-Si, in which each nucleus grows into one small grain in the final microstructure.

Unfortunately, a series of recent research results in laser-irradiated solidification experiments [52-54] reveal that such a material (i.e., fg-Si) is generated directly during rapid growth of solids. According to this defective-growth model, fg-Si is formed whenever the interfacial temperature at the rapid solidification front approaches, but is still above the interfacial amorphization threshold temperature [54]. Consequently the defect-rich microstructures observed upon irradiation at very low energy densities just above the surface melting threshold, could be accounted for by the defective growth model, since the interfacial temperature (close to the melting temperature of a-Si) of the growth front falls within the expected range of temperatures that correspond to

defective growth mode [52]. Nevertheless, we need to identify the details associated with the event that initiates the explosive crystallization (which in turn leads to the formation of fg-Si). In the following discussion, we argue that "sparsely distributed" heterogeneous nucleation of crystalline solid Si, taking place at the solid-liquid interface, corresponds to the explosive crystallization triggering process.

At energy densities above 90 mJ/cm^2, the most remarkable feature in the planar view TEM micrographs of the irradiated films corresponds to the radial disk-shaped regions (DSRs). At 90 mJ/cm^2, these DSRs have a very defective core area, which is surrounded by slightly less defective outer perimeters/region. This feature constitutes an important microstructural element that holds the key to unravelling the complex transformation details. Such a microstructural feature was not observed in laser irradiated microcrystal-rich LPCVD a-Si films [1], but has been previously reported in similar irradiation experiments conducted using a-Si layer obtained via heavy dose of ion-implantation [27].

At energy density of 109 mJ/cm^2 (Figure 4.2 (b)), the surface area can be identified as being mostly covered by radial DSRs, bordering one another. As the incident energy density increases (Figure 4.2 (c) and (d)), these DSRs become more prominent and discernable, and the diameter of the largest DSRs increases up to approximately 500nm. It is possible to

observe that DSRs in these energy densities consist of fg-Si core regions and relatively defect free boundaries/outer regions.

Additionally, it is possible to also note that in Figure 4.2 (d), the film surface is no longer fully covered by DSRs as we start to see some regions that consist of small equiaxed Si grains. Also at higher energy densities (Figure 4.3 (e) and (f)), we can notice that (1) the center regions of DSRs become less-defective and (2) the density of DSRs decreases. As the energy density increases, the fraction of the film covered with small equiaxed grains increases.

The sparsely distributed DSRs appearing in the microstructures, we argue, indicate that "sparsely distributed" nucleation of crystal Si (as opposed to copious volume filling nucleation of crystals proposed by the previous investigators) are the local triggering events that initiate subsequent solidification that generates fg-Si via defective crystal growth. Though one may argue that preexisting microcrystalline clusters in a-Si films (i.e., not nucleated crystals) can also be considered as the culprit, we suggest that such a notion can be excluded by the following points we can make after examining the films that are fully covered by DSRs. Firstly, within the corresponding energy density range, the observation that the number density of DSRs decreases as energy density increases is not what we would expect, since the increased energy density leads a prompt

formation of a deeper liquid layer, which in turn would lead to higher densities of DSRs. Secondly, the overall geometry of DSRs (for the case in which they mostly cover the entire film) doesn't suggest the Voronoi polygon geometry, the very configuration expected when they are essentially formed via near-simultaneous initiation of solidification from preexisting microcrystalline clusters.

The microstructural details associated with the DSRs also reveal how the growth of nucleated solids must have proceeded largely laterally into the surrounding liquid layer. This could be mostly accounted for by considering how the thermal conductivity of l-Si (~0.5 W/cm K) is significantly higher than that of the underlying a-Si (~0.02 W/cm K); both heat flow and the rapid crystal growth will therefore be well guided into the lateral direction. The laterally increasing crystallinity of DSRs can be subsequently explained as below: once nucleation of c-Si occurs, initially rapid and defective growth follows at undercooled interfacial temperature, producing defective c-Si; subsequently the growth of c-Si becomes slower, mainly as a result of interfacial recalescence in which the latent heat released by solidification warms the surrounding l-Si so as to reduce the degree of interfacial undercooling, thereby leading to the formation of less-defective c-Si.

At sufficiently higher energy densities, this can be followed by localized re-melting and re-solidification of the fg-Si regions and grain boundaries, leading to: (1) the formation of small equiaxed grains, and (2) less-defective material in the core regions of surviving DSRs. This scenario is also supported by the cross-sectional TEM images of the irradiated films at corresponding energy densities (Figure 4.3 (b), (c) and (d)). The clean grains in the outer perimeters of DSRs are formed via less-defective growth of liquid at raised interfacial temperatures resulting from latent heat released from the growth fronts of neighbouring DSRs, while the disappearance of fg-Si region in the center of DSRs (Figure 4.3 (d)) is an observation that suggests re-melting of the defective fg-Si cores that were formed immediately after crystal nucleation.

Experimental results obtained using AFM of irradiated samples are also consistent with the above observations and interpretations. Figure 4.4 shows that, at low energy densities (Figure 4.4 (a) and (b)), the DSRs can be clearly discerned and identified as covering most of the surface area; at much higher energy densities (Figure 4.4 (c) and (d)), small protrusions start to appear in the central regions of the DSRs as a result of localized re-melting of the defective core regions, and a substantial fraction of the surface area becomes covered with small equiaxed grains that, we argue, result from localized re-melting of the defective DSRs and grain boundaries from the DSRs that are formed much earlier.

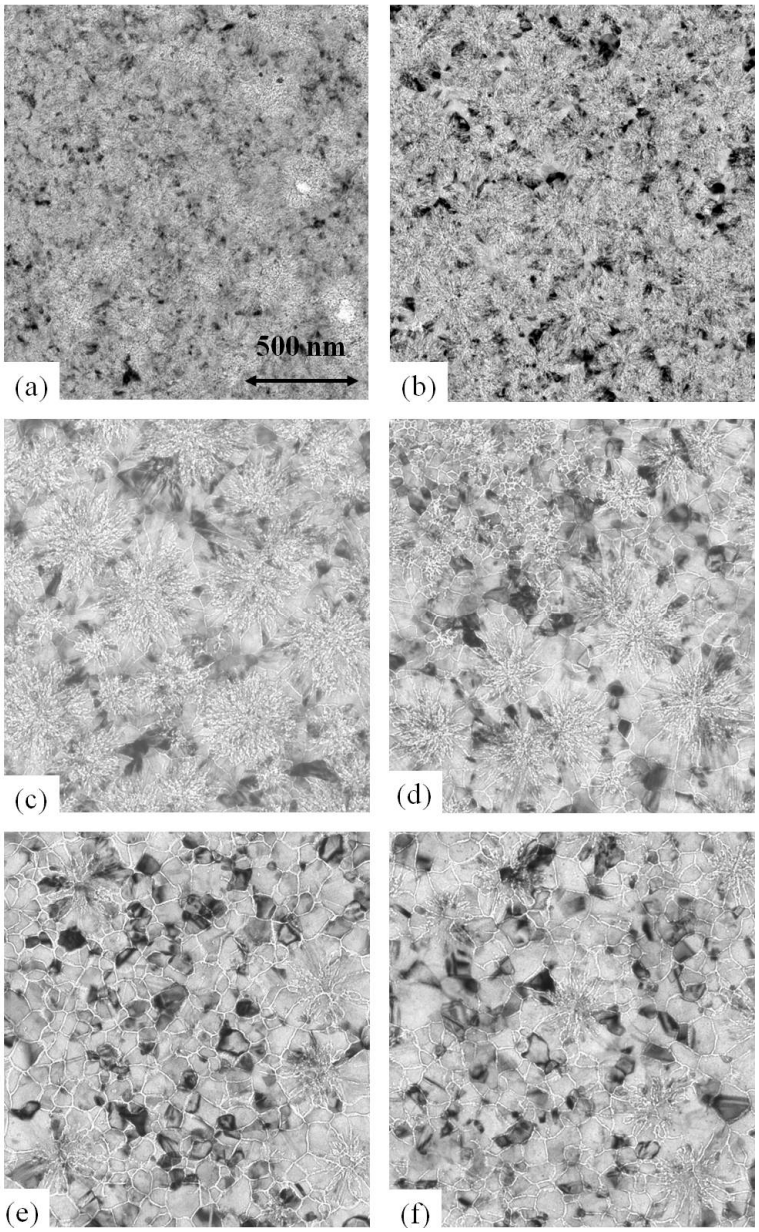

Figure 4.2 Planar view TEM images of 100nm dehydrogenated PECVD a-Si films single-shot irradiated at various energy densities: (a) 90 mJ/cm^2, (b) 109 mJ/cm^2, (c) 134 mJ/cm^2, (d) 171 mJ/cm^2, (e) 222 mJ/cm^2, (f) 238 mJ/cm^2. Complete melting threshold is 270 mJ/cm^2. Secco-etchant was used to enhance the surface grain boundary contrast.

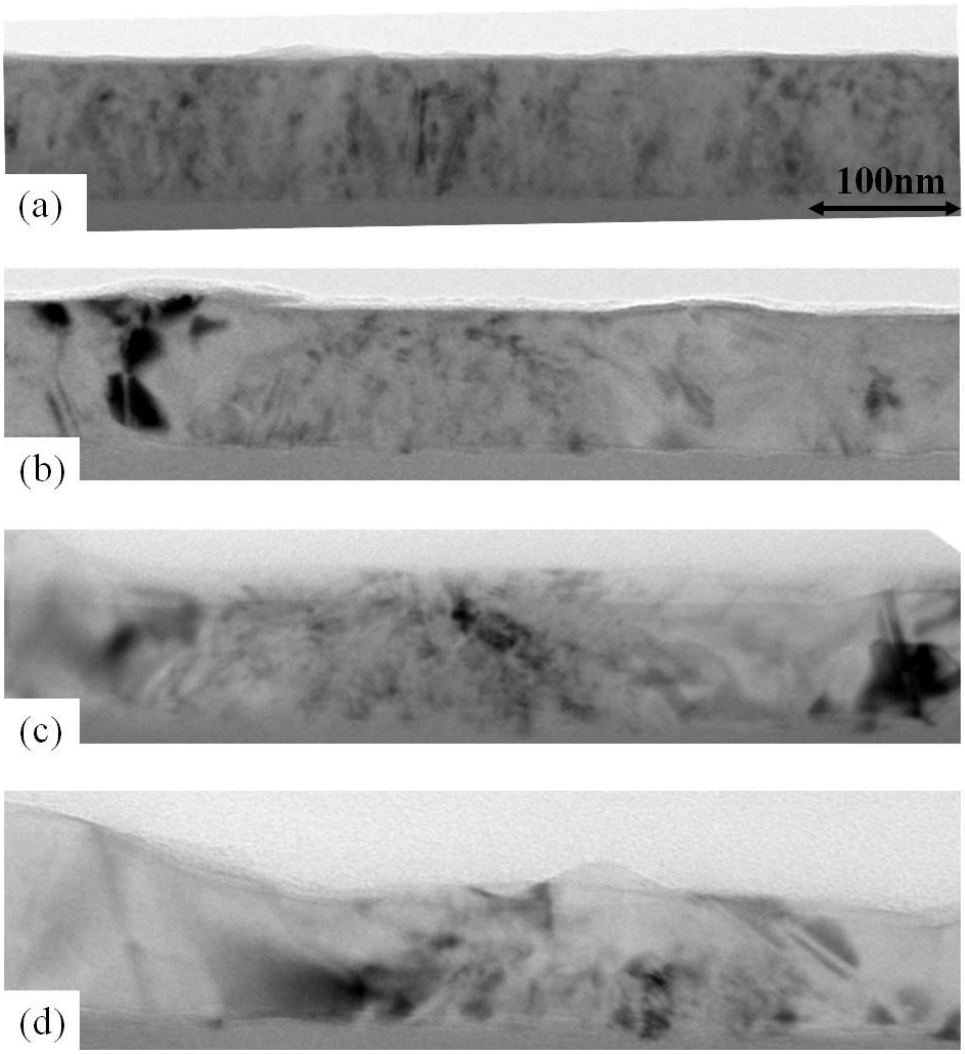

Figure 4.3 Cross-sectional view TEM images of 100nm dehydrogenated PECVD a-Si films single-shot irradiated at various energy densities: (a) 90 mJ/cm^2, (b) 109 mJ/cm^2, (c) 166 mJ/cm^2, (d) 236 mJ/cm^2. Complete melting threshold is 270 mJ/cm^2.

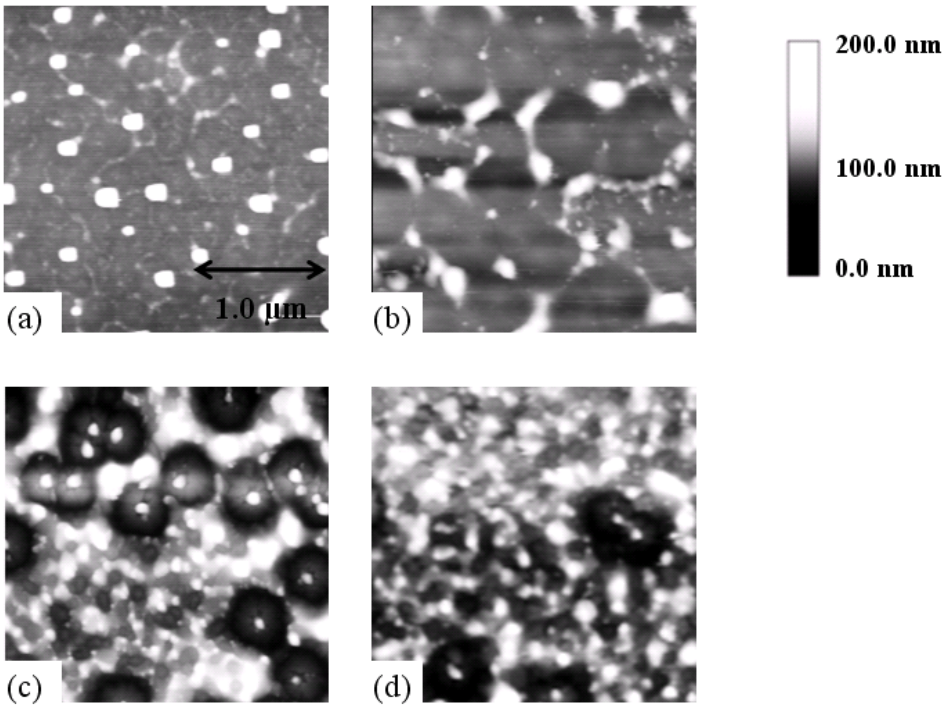

Figure 4.4 AFM images of 100nm dehydrogenated PECVD a-Si films single-shot irradiated at various energy densities: (a) 108 mJ/cm^2, (b) 150 mJ/cm^2, (c) 222 mJ/cm^2, (d) 238 mJ/cm^2. Complete melting threshold is 270 mJ/cm^2.

4.3.2 *In-situ* Transient Reflectance Analysis

As the liquid Si has a much higher reflectance than solid [55], the reflectance of the film must increase upon being melted. Therefore, front-side transient reflectance (FTR) measurement at visible wavelengths is an effective way to measure, among other things, the relative fraction of l-Si and c-Si in the near-surface region. Using these and transient conductance measurements, previous investigations [25, 27, 56-59] concluded that upon laser irradiation at energy densities in the partial melting regime, explosive crystallization takes place in the a-Si layer. According to a model proposed by Thompson *et al.* [25], a thin self-propagating buried liquid layer is formed as a result of the latent heat released when the primary melt begins to solidify at the maximum point of melting. To further assist analyzing the encountered situations, a back-side transient reflectance technique has also been developed and employed [60] to better reveal the dynamics of liquid-solid interface at deeper regions.

In this section, we present *in situ* experimental results obtained from employing front-side and back-side transient reflectance measurements to characterize the dynamics of melting and solidification in irradiated Si films.

Figures 4.5 and 4.6 show the time-resolved optical measurements obtained over a range of energy densities. Figures 4.7 and 4.8, on the other hand, show calculated oscillation behavior in reflectance obtained using thin-film multilayer interference reflectance model [61, 62] assuming that the film melts and solidifies in a one dimensional manner (i.e., uniform liquid layer is formed and solidified).

Figure 4.5 shows both the front-side and back-side time resolved reflectance of 100nm dehydrogenated PECVD a-Si films upon being irradiated at various energy densities. At the lowest energy density of 71.7 mJ/cm^2 below the surface melting threshold, the gradual changes in FTR and BTR signals can be explained by the temperature effect on optical refractive index of a-Si [16, 63]. For energy densities above the surface melting threshold, the FTR signal rises to a peak value when the film surface melts and decays as soon as solid appears in the near-surface region, since the skin depth of hot liquid Si at 650nm wavelength is ~ 10nm. However, this behavior in the FTR signal is distinct from what was previously observed with LPCVD a-Si films [1, 16] in which the FTR signal always exhibits a prompt and sharp peak/oscillation associated with early triggered explosive crystallization. Since as-deposited LPCVD a-Si film is known to contain a considerable number of preexisiting microcrystalline Si clusters [32, 64, 65], which contribute to the formation and propagation of a buried molten layer upon initial surface melting (i.e.,

the initiation of explosive crystallization), the observed behavior in FTR signals in the present experiments indirectly indicates that we can discount the existence of a large number of microcrystalline Si clusters in our dehydrogenated PECVD a-Si films.

Figure 4.6 shows a selection of FTR and BTR signals at six energy densities (selected from Figure 4.5). In Figure 4.6 (a), FTR signal shows a peak that indicates surface melting and a following dip which is viewed to be caused by the buried layer propagating into the a-Si [58]. The oscillation caused by interference of the light reflected at the surface and that reflected at the interface of the explosively propagating buried molten layer (Figure 4.7 (a)) is in good agreement with the values calculated based on thin film interference reflectance model [61, 62] (presented in Figure 4.7 (b)). Using the interference extremes in the signals, we can estimate the speed with which the buried molten layer propagates to be approximately 14 m/s; this value is in good agreement with previously reported explosive crystallization velocities [58, 66]. As expected, strong interference minima and maxima are also seen in the BTR signal and can be accounted for in a similar manner (Figure 4.7 (c)).

At "medium" energy densities of 134.6 and 165.7 mJ/cm^2 (Figure 4.6 (b) and (c)), we can note that the oscillation in the FTR signal disappears in the tail-side of the peak, while the peak itself becomes broader (which

indicates longer surface melt duration). The disappearance of oscillation indicates that the interference effect is no longer observed in the FTR signal as the surface melt becomes thicker and stays longer. The corresponding BTR signals, however (and as expected), show oscillations that result from the motion of the explosively propagating buried liquid layer (though in Figure 4.6 (c), an additional hump starts appearing in the tail). The hump in BTR signal becomes clearer and more prominent at higher energy densities (Figure 4.6 (d), (e) and (f)]; this strongly indicates that following explosive crystallization, a relatively simple and sufficiently one-dimensional vertical melting and re-growth is taking place (as shown by the calculation in Figure 4.8 (b)).

The behavior of FTR signals at higher energy densities (Figure 4.6 (d) and (e)) is more interesting and unexpected. As the incident energy density increases, a distinctive shoulder can be clearly observed in the falling portion of the FTR signals; this observation can be viewed as being supportive of the idea that some re-melting of initially solidified materials is actually taking place (since the beam is still on) even as the film predominantly and generally solidifies. In contrast, such decaying behavior in FTR signals has never been observed in pulsed laser melting of c-Si in which the FTR signals consists of a steep and abrupt decrease following a flat-topped plateau as one would expect for a uniform solid-liquid front vertically moving towards the surface. Only for energy

density above or equal to 247.0 mJ/cm^2 (Figure 4.6 (f)) can we observe a flat-topped plateau in FTR signal.

The time at which the first peak is reached in the FTR signal can be identified as describing the moment when optically significant fraction of solid regions (that originate from growth of nucleated solids) is formed in the near-surface melt region. Measured values of this time can be obtained from Figure 4.5, and are shown in Figure 4.10. The time of the initial peak in the FTR signal is found to decrease with increasing irradiation energy densities over the entire range of energy densities between 92.7 and 223.4 mJ/cm^2 within the partial melting regime. One important aspect is that this point always occurs before the beam is "turned off" (i.e., while the beam is still on). This means that initial nucleation events must take place while the laser pulse is still on. Especially for high energy densities above or equal to 181.4 mJ/cm^2, this measured time stays within 9.5 ± 0.5ns, close to time of the laser pulse peak at 8.4ns, and this strongly implies that solidification is initiated when the l-Si/a-Si interface is still moving at relatively high velocity (i.e., high melting rates). More details regarding estimation of the interface velocities and further explanation of the measured times will be discussed in Chapter 7 by using a one-dimensional numerical simulation analysis.

The results of the FTR and BTR signals presented above during melting and solidification can also be specifically correlated with the microstructural details presented in Section 4.3.1. As presented underneath, comparison of the *in situ* transient reflectance signals and planar view TEM micrographs (Figure 4.3), in fact, permits us to acquire a more detailed understanding of how a-Si melts and solidifies upon being partial-melted via laser irradiation.

At lower energy densities, oscillations in the BTR signals (Figure 4.6 (a), (b) and (c)) suggest explosive crystallization initiated by the initial solidification triggering events (i.e., formation of DSRs). As discussed before, the initial solidification starts at the center of DSRs, upon nucleation of crystals at the melting interface, and then promptly proceeds laterally via rapid and (at least initially) defective growth into the supercooled liquid Si, producing DSRs that fully cover the film surface (Figure 4.2 (a), (b) and (c)). Growth of DSRs in both the vertical and lateral directions reveals that solidification proceeds in a two-dimensional manner. This is reflected in the corresponding FTR signal as a gradual decay following the peak. Moreover, this also results in the non-planar interface of the explosively propagating buried molten layer, which destroys the strong interference-based signal oscillation, and makes it rather less meaningful to analyze the measured BTR signals using the thin film multilayer reflectance model. Therefore, in such a

situation involving more of two-dimensional melting and solidification, the dynamic information in FTR signals can be more effective in providing dynamic information than the BTR signals.

At higher energy densities, the unusual signal decaying behavior (i.e., the appearance of a distinctive shoulder in the FTR signal (Figure 4.6 (d) and (e)) can be viewed as supporting our TEM-based interpretation regarding the possibility of partial re-melting of the local regions of initially formed solids. This is to say that during the period in which overall solidification of the film transpires, at least within the optically accessible near-surface region of the film, the net rate of increase in the fraction of solid Si decreases (i.e., the liquid fraction decreases more slowly) compared to the situations that are encountered at lower energy densities. This is, according to our microstructure-based interpretation, caused by partial re-melting of fine-grained/defective Si regions and grain boundaries. As revealed in planar view TEM (Figure 4.2 (d) and (e)), cross-sectional view TEM (Figure 4.3 (c) and (d)) and AFM images (Figure 4.4 (c) and (d)), the localized re-melting of the originally very defective regions of DSRs (and grain boundaries) that were formed earlier leads to the formation of areas that consist mostly of small equiaxed grains, as well as less-defective core regions of surviving DSRs (which were formed later in the process). During this period, the laser is still providing sufficient energy that, re-melting of initially defective regions and grain boundaries with lower

effective melting points can occur concurrently with solidification of crystals proceeding into the surrounding undercooled liquid regions in the near-surface region that consist of a mixture of liquid and growing solid.

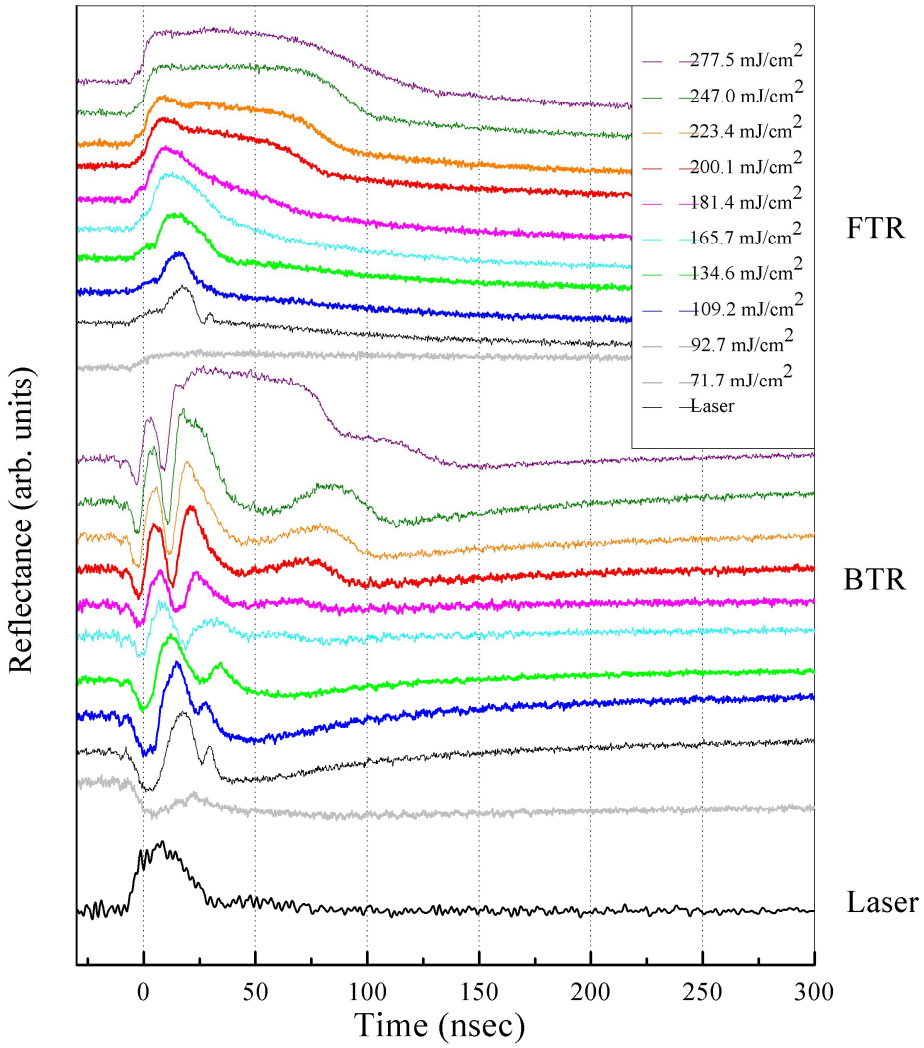

Figure 4.5 Front-side and back-side time resolved reflectance (in arbitrary units) at 650nm and 790nm wavelengths respectively of 100nm dehydrogenated PECVD a-Si film on glass substrate as a function of time and pulsed laser energy densities upon irradiation with a ~30ns FWHM pulse from a XeCl excimer laser. The laser starts at -10ns and the top of the laser pulse occurs at 8.4ns. Complete melting threshold is 270 mJ/cm².

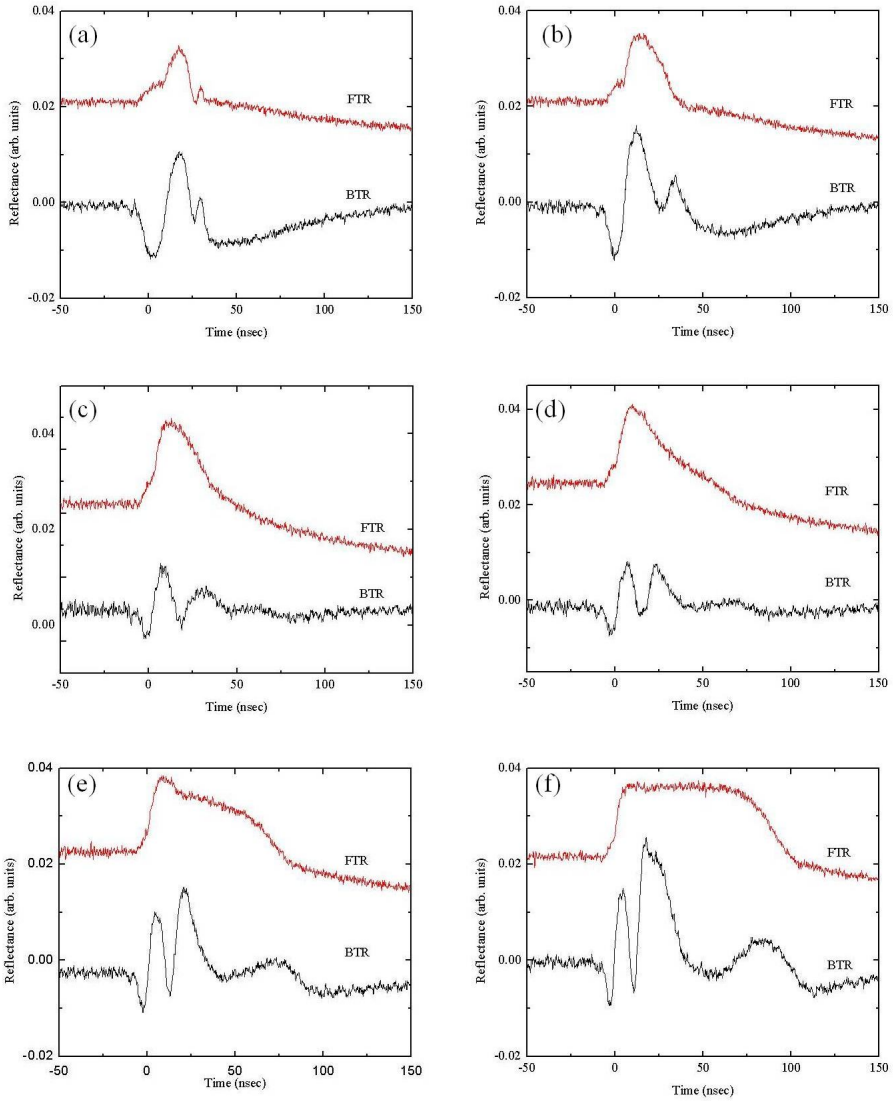

Figure 4.6 Front-side and back-side time resolved reflectance (in arbitrary units) at 650nm and 790nm wavelengths respectively of 100nm dehydrogenated PECVD a-Si film on glass substrate upon irradiation with a ~30ns FWHM pulse from a XeCl excimer laser at (a) 92.7 mJ/cm^2, (b) 134.6 mJ/cm^2, (c) 165.7 mJ/cm^2, (d) 181.4 mJ/cm^2, (e) 200.1 mJ/cm^2, (f) 247.0 mJ/cm^2. Complete melting threshold is 270 mJ/cm^2.

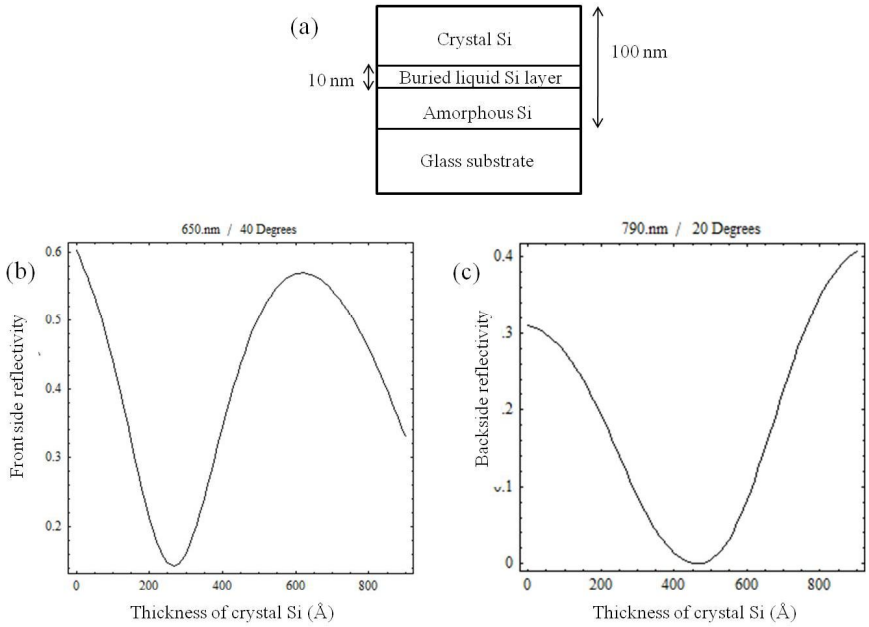

Figure 4.7 Calculation of reflectance based on thin film interference multilayer reflectance analysis. (a) Multilayered structure of 100nm Si thin film on glass substrate undergoing one dimensional solidification process under the assumption that a 10nm buried liquid Si layer propagates into a-Si, (b) Calculated front-side reflectance as a function of crystal Si thickness on top of the buried layer at 650nm wavelength, (c) Calculated back-side reflectance as a function of crystal Si thickness at 790nm wavelength. The optical index values of each material were taken from references [4, 5, 46, 67-69] at 1450K.

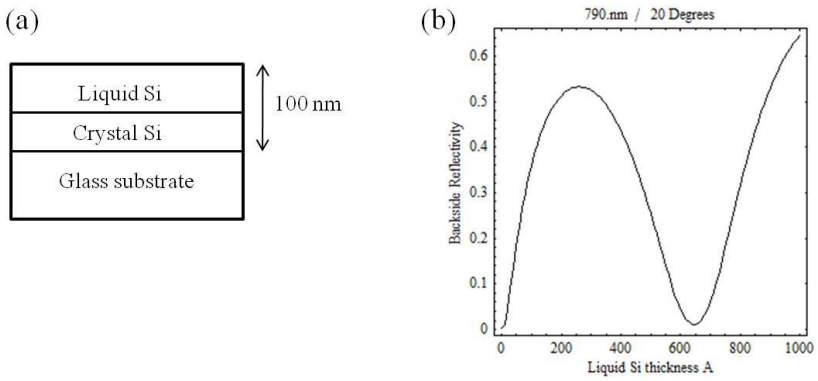

Figure 4.8 Calculation of back-side reflectance based on thin film interference multilayer reflectance analysis. (a) Multilayered structure of 100nm Si film on glass substrate that undergoes simple one dimensional vertical melting and solidification process: a liquid Si layer on top of crystal Si, (b) Calculated back-side reflectance as a function of remaining liquid Si thickness on top of the film at 790nm wavelength. The optical index values of each material were taken from references [4, 5, 46, 67-69] at 1450K.

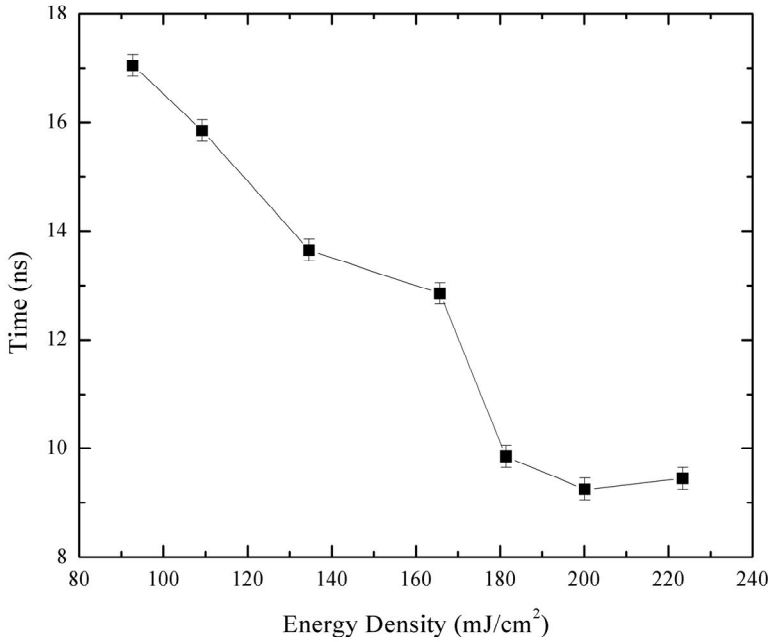

Figure 4.9 Measured times of the initial peak of front-side time resolved reflectance (as presented in Figure 4.5) at 650nm wavelength as a function of pulsed laser energy densities for 100nm dehydrogenated PECVD a-Si film on glass substrate upon irradiation with a ~30ns FWHM pulse from a XeCl excimer laser. A shown in Figure 4.5, the laser starts at -10ns, reaches the peak intensity at 8.4ns, shuts off after 30ns. Complete melting threshold is 270 mJ/cm^2.

4.4 Additional Discussions

4.4.1 Melting and Solidification Scenarios

Based on our experimental findings and recent progress in understanding of the direct growth model, we identify the following melting and solidification sequence for single-shot irradiated microcrystalline-cluster-deficient a-Si films in the partial melting regime.

(1) Upon irradiation by laser pulse above the surface melting threshold, a-Si film directly melts, producing a near-surface pool of l-Si undercooled relative to melting point of crystal Si.

(2) Later at some point during melting of a-Si film, solidification is triggered by spatially dispersed nucleation of crystalline Si seeds.

(3) Once nucleated, c-Si grows vertically and laterally into the undercooled liquid layer, initially in the mode of defective growth, forming the defective Si regions with the fine-grained microstructure.

(4) As latent heat released from the crystal Si growth induces the melting of the underlying a-Si layer, vertical and lateral explosive crystallization takes place and proceeds into a-Si.

(5) As solidification proceeds, the latent heat of transformation/fusion released at the interface (i.e., interfacial recalescence) increases the interface temperature, and this subsequently leads to crystal growth via epitaxial (i.e., significantly less-defective) mode of growth that leads to the formation of the "clean" outer perimeters of the DSRs.

(6) At sufficiently high energy densities, the laser beam assists local preferential re-melting of the defective regions and grain boundaries, which leads to the formation of less-defective small equiaxed grains and surviving/later-formed DSRs with less defective core regions.

4.4.2 Nucleation Mechanism

From the detailed study of post-irradiation resulting microstructures in Section 4.3.1, we propose that nucleation of crystal Si is responsible for triggering explosive crystallization and defective growth. If so, then we need to answer a fundamental question regarding the nucleation mechanism of crystalline Si: when and where does the nucleation take place?

Referring to Figure 4.9, we demonstrate that initial solidification (nucleation of c-Si) occurs even when a-Si is being melted and laser beam

is still on. Especially at sufficiently higher temperature, the onset of nucleation takes place around the peak of the laser which corresponds to the essentially maximum velocity of l-Si/a-Si interface. This is very different from the description presented previously [25, 70] in which upon laser irradiation with short pulse duration (< 30ns FWHM) solidification is identified to start only when the melt reaches its maximum depth (i.e., the interface becomes essentially stationary) after the incident laser pulse essentially decays (i.e., the beam is essentially "off").

As for the nature of nucleation occurring during partial melting irradiation of a-Si, we can safely exclude homogeneous nucleation in the undercooled bulk liquid Si [43, 71-74], given that the film is still being heated by the beam at the onset of nucleation (and therefore the degree of supercooling reached is at least two hundred degrees higher than has been identified experimentally for these time scales). While it is also impossible for nucleation to occur at the surface (refer to Appendix A for further explanation), the only realistic interface available for heterogeneous nucleation to take place is at the moving interface between a-Si and l-Si.

Our proposed model involving heterogeneous nucleation of crystals at the melting interface may be incorrectly be viewed as being similar to the

Tsao/Peercy model [28], but these two models are in fact substantially quite different. The model proposed by Tsao *et al* assumes that copious (not "spatially sparse" but "sufficiently copious" to essentially volumetrically fill up the material at the nano-scale) nucleation takes place continuously during the entire explosive crystallization process to account for both the triggering and sustaining of explosive crystallization. (Here it is assumed incorrectly that each nucleation event corresponds to one grain in the fine-grained polycrystalline Si microstructure.)

4.4.3 Comparison with Previous Investigations

The most significant microstructural feature that forms the basis for our interpretation corresponds to the DSRs, which consist of defective cores and less-defective outer perimeters (Figure 4.11 (a)). To account for the formation of DSRs, we propose that after spatially distributed nucleation of c-Si occurring at the moving l-Si/a-Si interface, initially rapid and defective growth proceeds primarily laterally, generating the fine-grained polycrystalline Si in the core regions of DSRs, while less-defective grains in the outer perimeter result from interfacial recalescence as solidification proceeds along the lateral direction.

As it happens, such a microstructure feature has been previously observed by two research groups; however, they have accounted for it in

using transformation scenarios that are different from what we are proposing in this thesis. We'll review their models and discuss how our present conclusions are fundamentally distinct from previous models.

Lowndes *et al* [27] first report this feature (Figure 4.10 (b)) in the course of studying pulsed laser induced crystallization of a-Si layer formed via ion irradiation of Si wafer. They suggest that the DSRs (referred to as "flakes" in their work) are responsible for initiating explosive crystallization (as we also suggest in the present work). However, an important point mentioned within their work pertains to their insistence that the cores of the regions are amorphous. This insistence, in turn, prevents one from stating that nucleation of crystal Si is what initiated the formation of these structures (as amorphous cannot "nucleate and grow" on the identical material!), the very point that forms the most important ingredient in our model.

Recently Mariucci *et al* [45] also present a similar microstructure feature (Figure 4.10 (c)) during the investigation of as-deposited PECVD a-Si films. However, without providing any explanation of the initial solidification events that trigger explosive crystallization, they assumed quite incorrectly that explosive crystallization always takes place very early and promptly, so that a-Si is nearly instantaneously converted into the fine-grained Si layer. This scenario is found to be the case for

microcrystalline-clusters-rich as-deposited LPCVD a-Si films [16, 32] (wherein explosive crystallization is promptly triggered by the growth of embedded microcrystalline Si clusters into the surrounding undercooled melt), it is not valid for microcrystalline-clusters-deficient a-Si films with which explosive crystallization can only be triggered by nucleation of c-Si. Under this invalid assumption they have made (which partially resulted from not having carried out any FTR measurements), they propose a physically inconsistent and incorrect model that argue that these disk-structures are formed by the simple re-growth from the uniformly melted fine-grained polycrystalline Si layer.

4.5 Summary

In this chapter we have investigated partial melting and solidification of dehydrogenated PECVD a-Si films upon single-shot short pulse laser irradiation (FWHM < 30ns) at various energy densities. Extensive *in situ* transformation analysis was performed using both front-side and back-side transient reflectance measurements and microstructural characterization of the irradiated films was conducted using TEM and AFM.

Both *in situ* optical measurements and microstructural analysis indicate a two-dimensional melting and solidification scenario, distinct from what was observed with microcrystalline-cluster-rich as-deposited LPCVD a-Si films. In particular, AFM and TEM analyses reveal the presence of disk-shaped regions (DSRs) that have defective core areas and less defective outer perimeters. Based on the above observation, we identify some of the fundamental factors that can participate and affect the ways a-Si can melt and solidify: (1) the occurrence of spatially dispersed and temporally stochastic nucleation of crystalline solids at the moving liquid-amorphous interface, (2) the formation of fine-grained Si through very defective crystal growth proceeding, at least initially after nucleation, at crystal solidification fronts moving at certain sufficient rates, and (3) the propensity for local preferential re-melting (while the beam is still on) of defective regions and grain boundaries.

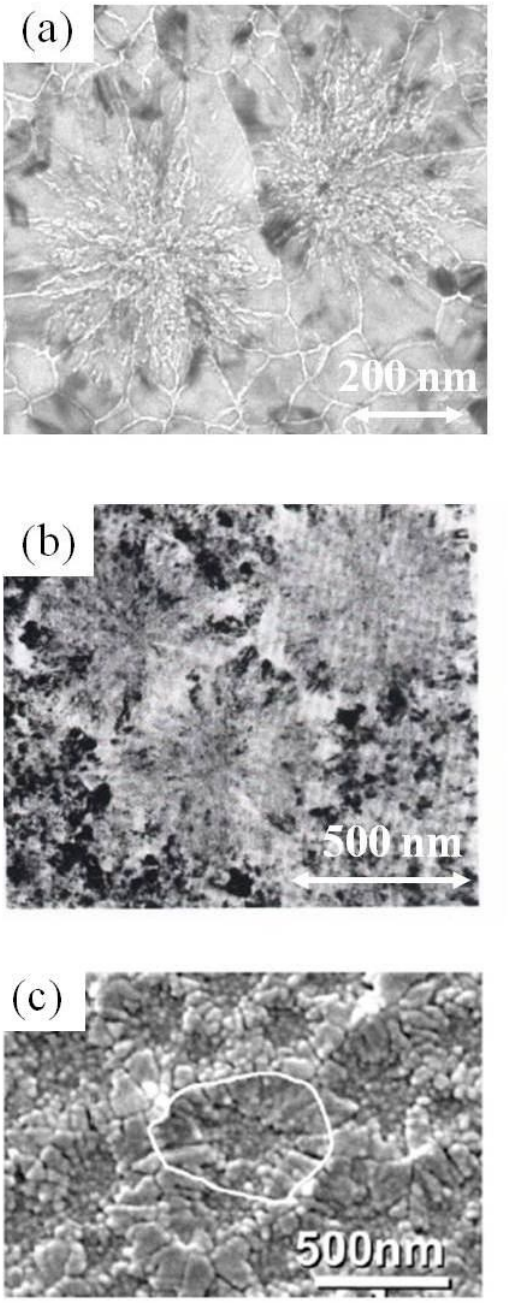

Figure 4.10 Disk Shaped Regions (DSRs) obtained upon single-shot laser irradiation. (a) planar view TEM image from Figure 4.2 (d), (b) planar view TEM image from reference [27] showing flakes, (c) SEM micrograph showing disk-like structure as presented in reference [45].

Chapter 5 Pulsed Laser Crystallization of PECVD a-Si Films: Double Gaussian Pulse Irradiation

5.1 Introduction

In Chapter 4, we focused on studying the dynamics of melting and solidification of dehydrogenated PECVD a-Si films irradiated with a "simple" laser pulse (i.e., temporal profile with a single peak) (Figure 4.1). However, in order to increase the power, many industrial systems operate with pulses with a slightly more complex temporal profile. One can increase the power by optimizing the reactive gas concentration in the laser gas mixture. This produces, however, a temporal profile with a smaller second hump following the first peak (Figure 5.1). (This effect is known to be inherent to the Lambda Physik LPX 315i XeCl excimer laser at 308nm wavelength [75].) As the profile of a pulse can potentially affect the details associated with how amorphous Si can melt and solidify, and as the industrial usage of such a beam to crystallize dehydrogenated PECVD a-Si films demand that we understand such details to improve

the crystallization process. In this chapter we examine the effects that result from irradiating a-Si films with such a beam with the double-peak pulse temporal profile.

Both the time resolved optical signals and the microstructural analysis suggest that the second hump in the laser temporal profile largely enhance and strengthen the re-melting part of the process. This leads to a set of resulting microstructures that are largely similar yet clearly distinct from those observed using a single peak pulse temporal profile (Section 4.3.1). We will also cover the implications of these findings on the ELA (i.e., excimer-laser annealing) method and the possibility of developing partial-melting-regime-based ultra-high-throughput crystallization methods.

5.2 Experimental Details

The XeCl excimer laser system operates at 308nm wavelength, with a double-peak temporal profile as shown in Figure 5.1. The full-width at half maximum (FWHM) of the pulse is around 30ns. *In situ* time resolved optical measurements (both front-side and back-side reflectance analysis) were performed using the signals, monitored with probing lasers at

675nm wavelength. Microstructural characterization of the irradiated films was performed using planar TEM, cross-sectional TEM and AFM.

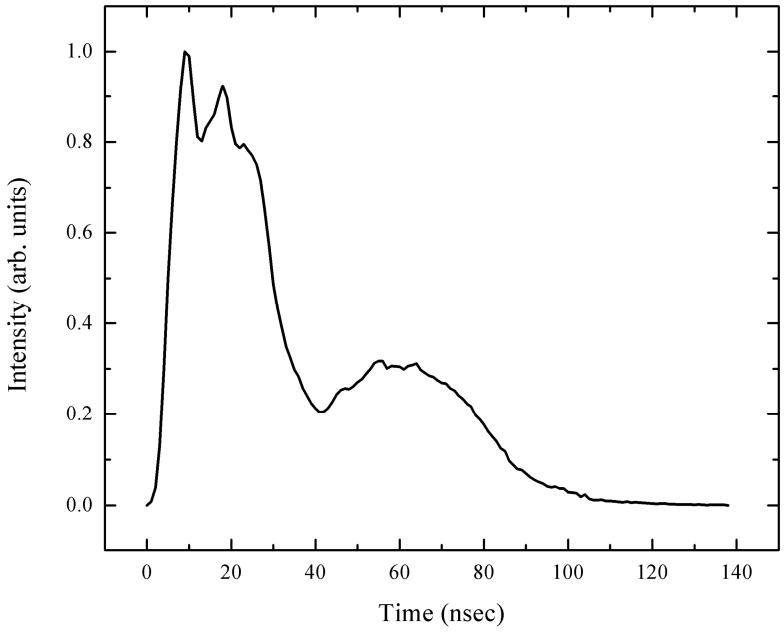

Figure 5.1 Temporal profile of irradiation laser pulse (308nm, FWHM ~30ns).

5.3 Experimental Results

5.3.1 Microstructure Analysis

Figure 5.2 and Figure 5.3 show the resulting microstructures of a-Si films irradiated at various energy densities. Planar TEM micrographs reveal that at low energy densities just above the melting threshold (Figure 5.2 (a)), we observe a very defective/fine-grained microstructure largely similar to what was shown in Figure 4.2 (a). This microstructure could just as well be explained as resulting from nucleation of crystal Si occurring at the l-Si/a-Si interface subsequently leading to defective crystal growth in lateral and vertical directions. Due to the significantly higher velocity expected in the lateral solidification, the overall microstructure is expected to demonstrate mostly one dimensional growth; such a microstructure that revealing a mostly one-dimensional-growth microstructural signature is manifested in the cross-sectional TEM micrograph shown in Figure 5.3 (a) as defect-rich columnar structure.

In general, as energy density increases (Figure 5.2 (b) (c) and (d)), the grains tend to become cleaner and larger. The corresponding cross-sectional TEM images (Figure 5.3 (b) and (c)), show the grains near the film surface are noticeably larger and cleaner than those near the bottom

substrate interface, strongly imply that the film surface has undergone substantial re-melting. Only at sufficiently higher energy densities (Figure 5.2 (d)) do we observe discernible radial disk-shaped regions (DSRs) that have less-defective core regions resulting from re-melting.

One important observation from the planar view TEM microstructural analysis is that under low-energy-density irradiation, the DSRs that were clearly discernible previously with a single-peak pulse (Figure 4.2) become largely absent in the samples irradiated with a double-peak profile (Figure 5.2 (a), (b) and (c)). This conclusion is further confirmed and assisted by the difficulty with which the DSRs can be identified in both cross-sectional TEM and AFM images (Figure 5.3 and Figure 5.4). Since the second peak in the laser pulse profile brings extra laser energy at a delayed time, re-melting would be expected to occur at some point when the laser energy absorbed by the solidified materials is sufficient to heat the materials above the melting point. Given that the effective melting point of defective/fine-grained Si is lower than that of single crystal Si (1685K), we would anticipate that defective/fine-grained Si is more prone to be re-melted. At low energy densities, the first peak within the laser pulse could possibly fully convert a-Si film into defective/fine–grained Si similar to Fig 4.2 (a), while the second peak could induce re-melting of the initially solidified Si, producing less-defective grains near the surface region as shown in Figure 5.2 (b).

As the energy density increases (Figure 5.2 (c) and (d)), more energy will be absorbed by the initially solidified materials so that the grain boundaries/fg-Si could be re-melted in a more substantial manner, leading to the formation of larger and cleaner grains in the resulting microstructure.

The detailed microstructural characteristics of the DSRs in Figure 5.2 (d) can also be accounted for by using the melting and solidification sequence presented in Section 4.4.1. At sufficiently high energy densities (Figure 5.2 (d)), within the first peak of the pulse temporal profile, spatially dispersed nucleation of c-Si occurs at the moving l-Si/a-Si interface; producing "presumably and transiently" distinguishable DSRs (similar to Figure 4.2 (c), with diameters even larger than the film thickness). Subsequent energy deposition by the second hump would induce prompt re-melting of the defective cores in the DSRs, leading to the formation of "modified" DSRs with less-defective core areas. This accounts for the observed TEM micrograph (Figure 5.2 (d)), though in the corresponding AFM image (Figure 5.4) the DSRs are not so distinguishable, (due presumably also to the enhanced re-melting of the entire surface of the film and smearing the surface topological signature caused during lateral growth of the DSRs). More information about (1) the time at which nucleation transpires and (2) enhanced re-melting of the material could be

inferred from *in situ* transient reflectance analysis (and will be discussed in the following section).

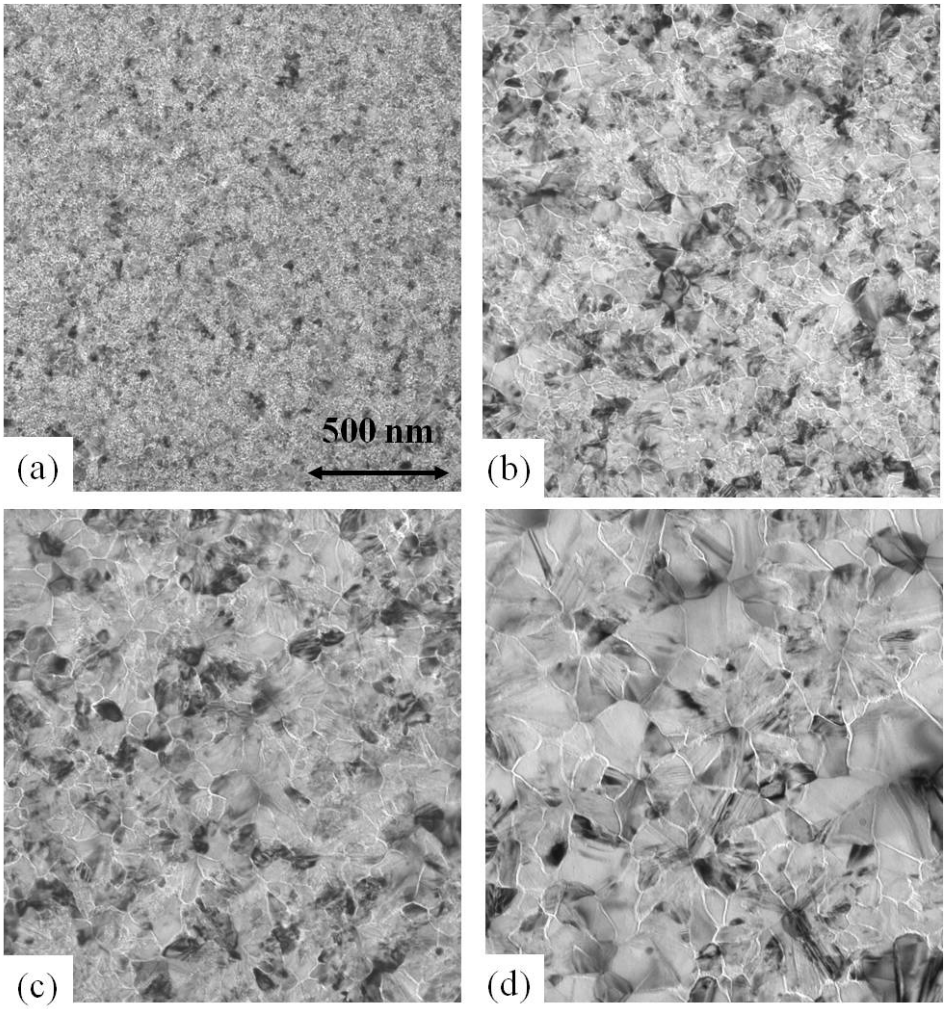

Figure 5.2 Planar view TEM images of 100nm dehydrogenated PECVD a-Si films irradiated various energy densities: (a) 192.7 mJ/cm^2, (b) 240.9 mJ/cm^2, (c) 273.0 mJ/cm^2, (d) 325.2 mJ/cm^2. Complete melting threshold is 401.5 mJ/cm^2. Secco-etchant was used to enhance the surface grain boundary contrast.

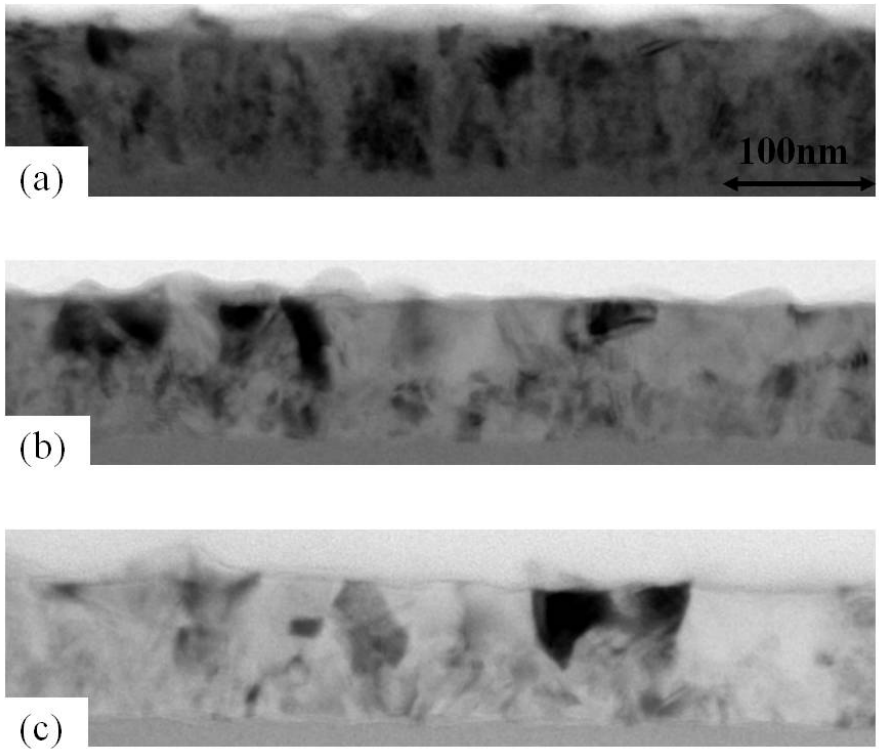

Figure 5.3 Cross-sectional view TEM images of 100nm dehydrogenated PECVD a-Si films single-shot irradiated at various energy densities: (a) 208.8 mJ/cm^2, (b) 240.9 mJ/cm^2, (c) 261.0 mJ/cm^2. Complete melting threshold is 401.5 mJ/cm^2.

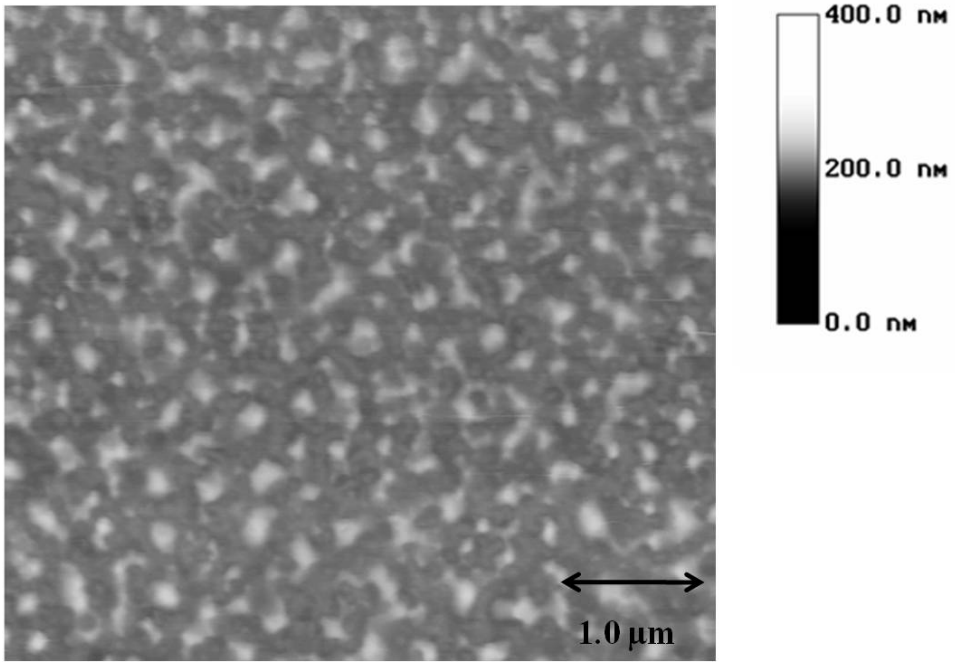

Figure 5.4 AFM image of 100nm dehydrogenated PECVD a-Si films single-shot irradiated at the energy density of 313.2 mJ/cm^2, corresponding to the microstructure shown in Figure 5.2 (d). Areas in white represent higher surface regions than those in black, as it is defined in the experimental setup.

5.3.2 *In situ* Transient Reflectance Analysis

As discussed in Section 4.3.1, a-Si can melt and solidify in a two dimensional manner once nucleation of c-Si occurs at the moving l-Si/a-Si interface. We also concluded in Chapter 4 that with two-dimensional melting and solidification, the FTR signals can be effective in analyzing the dynamics compared to the BTR signals (which becomes over complicated as a number of signals affecting factors compound and contribute). Therefore, we'll focus on analyzing FTR signals in this section to decipher the details associated with melting and solidification.

Figure 5.5 shows the representative FTR signal obtained from the 100nm dehydrogenated PECVD a-Si films upon irradiation with double peak laser pulse profile. Distinct from what was observed with single peak laser irradiation in Section 4.3.2, the FTR signal clearly exhibits two FTR signal humps, that more-or-less follows the overall temporal shape of the laser profile. This correlated behavior indicates that the film undergoes definitive re-melting as it is affected by energy deposition that results from the second peak in the incident beam.

Figure 5.6 presents both FTR and BTR signals of irradiated a-Si films at various energy densities. As was expected, the noisy and indiscernible oscillations seen in the BTR signals make the detailed analysis rather

difficult and meaningless. On the other hand, important information can be extracted in a straight forward manner from the FTR signals.

Figure 5.7 plots two characteristic times measured from FTR signals in Figure 5.6. The first extracted point corresponds to the time of the first peak of FTR signal, correlating to the time at which optically significant fraction of solid regions (initiated from heterogeneous nucleation of solids taking place at the interface) are established in the near-surface region. Since solidification must be initiated by the nucleation events occurring at the moving l-Si/a-Si interface, this time also determines the time scale associated with initial nucleation. The second point extracted from the plot is the time associated with the dip in FTR signal that reflects the time at which significant surface re-melting starts to take place. FTR signal reaches the valley as soon as the solidification proceeds to a maximum extent before the film surface starts to be re-melted.

As shown in Figure 5.7, the "initial peak" time is found to decrease with increasing energy density. In other words, nucleation of c-Si starts to occur earlier as the energy density actually increases. This trend is similar to what was observed in Section 4.3.2. As for the time at which the FTR signal reaches the dip, the measured value is almost and effectively constant at around 41 ± 2ns (within the second hump portion of the laser profile), over the range of energy densities ranging from 212.8 mJ/cm^2 to

377.4 mJ/cm^2. More details concerning the implications that can be inferred from Figure 5.7 will be discussed by employing numerical simulation analysis in Chapter 7.

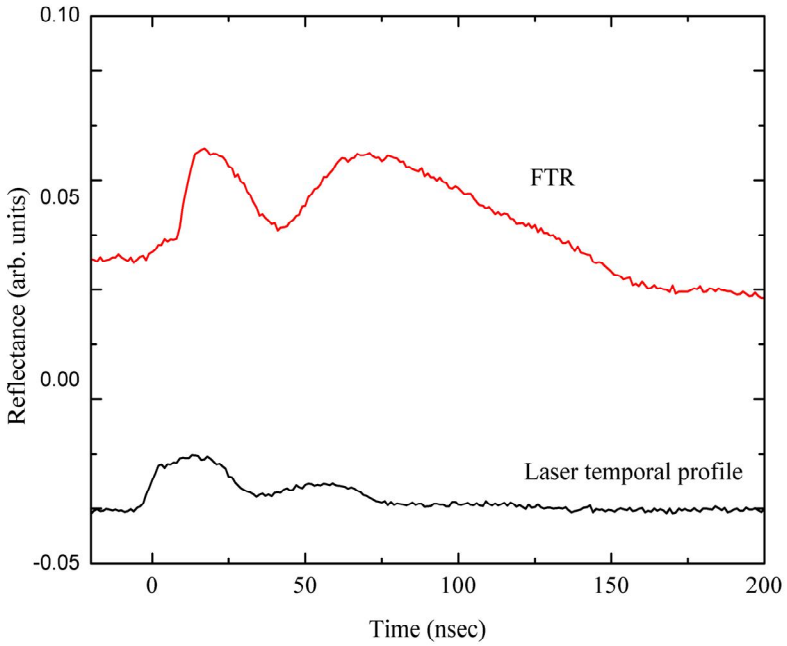

Figure 5.5 Front-side time resolved reflectance (in arbitrary units) at 670nm wavelength of 100nm dehydrogenated PECVD a-Si film on glass substrate as a function of time upon irraidation with a double-peak laser pulse from a XeCl excimer laser at pulsed laser energy density of 324.5 mJ/cm^2. Complet melting threshold is 401.5 mJ/cm^2.

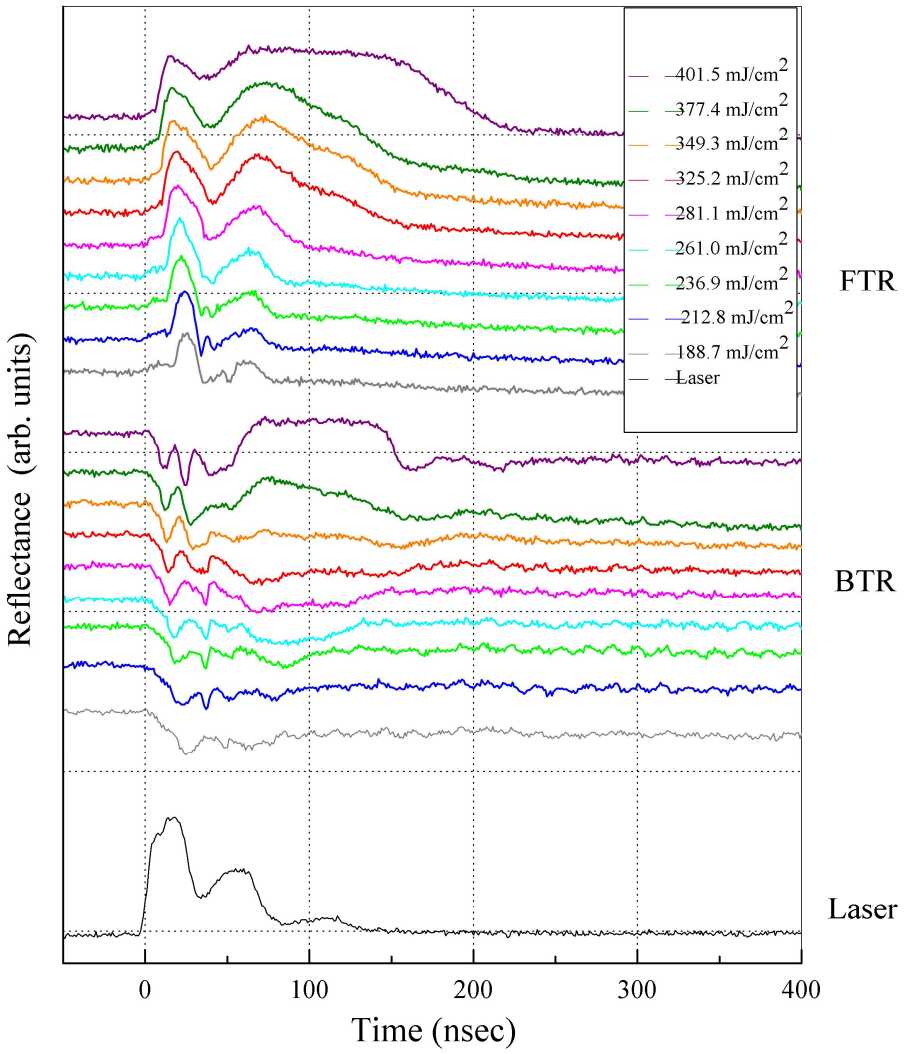

Figure 5.6 Front-side and back-side time resolved reflectance (in arbitrary units) at 675nm wavelength of 100nm dehydrogenated PECVD a-Si film on glass substrate as a function of time and pulsed laser energy densities upon irradiation with a double-peak laser pulse from a XeCl excimer laser. The laser starts at -4ns and reaches the first peak at 15ns, the first minumum at 34ns, and the second peak at 54ns. Complete melting threshold is 401.5 mJ/cm².

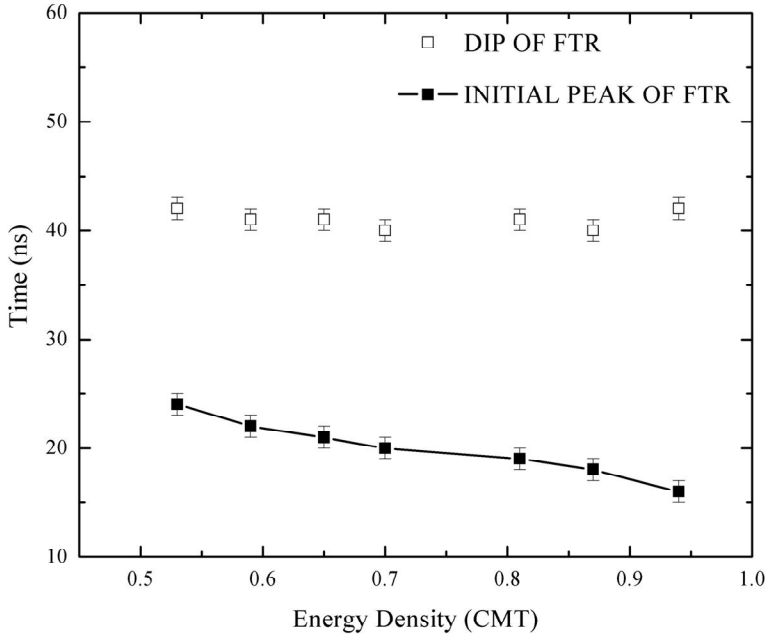

Figure 5.7 Measured times of the initial peak and the dip of front-side time resolved reflectance (as presented in Figure 5.6) at 675nm wavelength as a function of pulsed laser energy densities for 100nm dehydrogenated PECVD a-Si film on glass substrate upon irradiation with a double-peak laser pulse from a XeCl excimer laser. A shown in Figure 5.6, the laser starts at -4ns and reaches the first peak at 15ns, the first minumum at 34ns, and the second peak at 54ns. The energy density is calibrated by complete melting threshold (CMT) which is 401.5 mJ/cm^2 for this set of experiments.

5.4 Additional Discussions

5.4.1 Second-Peak-induced Re-melting of the Films

In this section we will first review the re-melting process upon laser irradiation with single pulse profile, and then compare that situation with the situation constructed using the results presented in this chapter to elucidate the effect resulting from the second peak (regarding the beam-assisted re-melting of the film).

As we concluded in Section 4.3, re-melting is an important step that can convert defective/fine-grained Si materials into a region consisting of less-defective grains, and can, therefore, definitively affect the microstructural formation of the irradiated films. In Section 4.3.2, we presented how re-melting could slow down the decay of FTR signal and even be recorded in FTR signal as a distinctive shoulder (appearing after the initial peak in profile). In the previous case, prominent re-melting was detected only at sufficiently high incident laser energy densities. It is also noteworthy that re-melting of defective/fine-grained Si occurs relatively concurrently with the formation (via solidification) of less-defective/cleaner Si in the epitaxial mode of growth.

On the other hand, we can conclude that, from the experimental results presented in the previous section in this chapter, significant re-melting is taking place over almost the entire energy density range, within the partial melting regime. Specifically, the second peak in FTR signal corresponds to the re-melting and re-solidification within the second peak in laser temporal profile. Moreover, the steep and abrupt fall following the first peak of FTR signal suggests that, during the initial solidification process, no significant re-melting is taking place. This further implies that re-melting induced by the second peak in laser profile occurs at a later time when the initial solidification stops, in contrast to "concurrent and simultaneous" re-melting often accompanied by solidification with single-peak laser-profile irradiation.

These observations demonstrate how slight modifications in the shape of the laser temporal profile can profoundly affect the specific sequence and details of melting and solidification (and, therefore, also the resulting microstructures).

5.4.2 Implications on the ELA Method

Excimer Laser Annealing (ELA) is a partial-melting based crystallization method that is presently and extensively being used for making low-temperature polycrystalline Si (LTPS) TFTs, which are needed in manufacturing high quality LCDs and AMOLED displays [76, 77]. Attaining the necessary level of device performance requires polycrystalline Si films with a uniform microstructure. The present state-of-the-art ELA system/process requires irradiation of the films with a substantial number of shots (approximately, and often greater than, 20 times) that severely restricts the capacity throughput per system. The efforts to reduce the number of pulses per area needed to attain the uniformly microstructured and sufficiently high-performance-enabling material is viewed as being very important for the future growth potential of the field.

The results we have presented in this chapter (which looked specifically into the temporal profile found in high-powered excimer lasers) can, we suspect, have profound implications regarding the future evolution of the field. Specifically, we have found that the presence and optimization of the second peak can be used to manipulate the re-melting process. When implemented properly, this may lead to the formation of uniform low-defect-density large-grained Si films.

Based on these results of single-shot irradiation, it is possible to understand the critical crystallization-related details associated with the all-important first-shot irradiation in the ELA process. This is well recognized as being extremely important information needed for improving the efficiency of the method, and which was lacking prior to this investigation. (In general, the microstructure obtained after the first shot profoundly affects the subsequent microstructure evolution manifested during the ELA process.) By optimizing the "first shot" crystallization step, we anticipate that the barrier associated with the present ELA method can be potentially overcome. Ultimately, by optimizing the temporal profile to control the nucleation initiated solidification with the first pulse, and the re-melting of the films using the second peak, it is also possible to envision a novel partial melting-based crystallization method that may ultimately require just a single shot. Such a method may utilize two pulses generated from two separate lasers or from a single laser pulse.

5.5 Summary

In this chapter we have analyzed the melting and solidification dynamics encountered during the laser irradiation of dehydrogenated PECVD a-Si films using a pulse with a double-peak temporal profile. The

experimental results, which are distinct from those obtained using a single-peak pulse, are nonetheless consistent with, and supportive of, the working model we have developed to account for the single-peak results. The most noteworthy (and expected) result is that the second peak in the laser profile can substantially enhance the re-melting process throughout essentially the entire energy density range. (Such identifiable re-melting, in contrast, was found to only occur at higher energy densities with single peak laser profile irradiation (Section 4.4).)

The findings are at least relevant to understanding and optimizing the ELA method, leading to the possibility of developing a partial-melting-regime-based ultra-high-throughput crystallization method.

Chapter 6 Pulsed Laser Crystallization of PECVD a-Si Films: Long Pulse Irradiation

6.1 Introduction

In Chapters 4 and 5, we have investigated the melt-mediated transformation details that arise when dehydrogenated PECVD a-Si films are single-shot irradiated with a short-duration pulse (308nm, FWHM ~30ns). In this chapter, we examine the situation involving irradiation of the same films (dehydrogenated PECVD Si) with a substantially long pulse duration pulse. We are motivated to study the possible variations in the melting and solidification dynamics, induced by introducing such a change for engineering-related and transformation-investigation-related reasons. For instance, it is technologically possible to introduce such a change by introducing a simple optical pulse-duration extender. This being so, if the modification leads to the changes that increase the efficiency and/or effectiveness of the ELA method, then it can be a simple

and elegant way to improve the method. (Previous investigations have not definitively clarified the potential benefits or penalties associated using long duration (150-250ns) pulses [78-81].) Scientifically, a number of kinetic steps involved in the transitions will likely be affected in ways that may help us not only understand what happens when long duration pulses are employed, but, more significantly, may permit us to critically examine and further refine the scenarios we have developed in the previous chapters.

In this chapter, we present our experimental findings using long pulse irradiation (FWHM ~ 240ns). These findings, combined with previous studies using short pulse irradiation (FWHM ~ 30ns), lead us to develop a deeper understanding of melting and solidification details of microcrystalline-clusters-deficient a-Si films partial-melting irradiated with different pulse durations.

6.2 Experimental Details

The pulse duration of an excimer laser can be extended up to 8 times the original pulse duration by putting a pulse duration extender (Exitech, Inc.) before the attenuator in Figure 3.1. The device [82] uses an array of mirrors to split and delay the original input pulse, this creates a series of

slightly overlapping pulses and leads to the extension of the original input pulse. The temporal profile used in this chapter is shown in Figure 6.1. Both front-side and back-side transient reflectance measurements were carried out at 675nm wavelength, at an incident angle of 40^{o} and 20^{o}, respectively. We have employed the similar experimental techniques as presented in the previous chapters (i.e., both *in situ* transient reflectance measurements and microstructural characterization of post-irradiation films were performed).

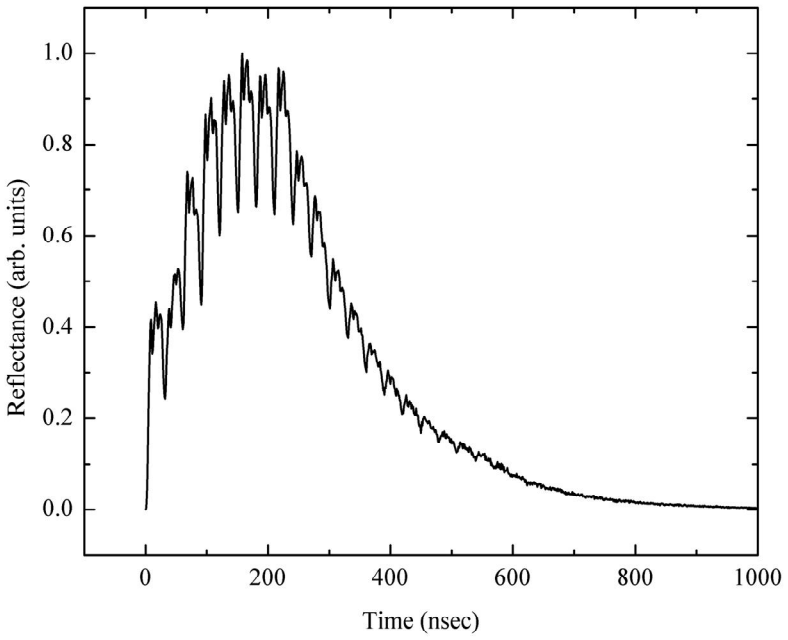

Figure 6.1 Temporal profile of irradiation laser pulse (308nm, FWHM ~240ns).

6.3 Experimental Results

6.3.1 *In situ* Transient Reflectance Analysis

Figure 6.2 shows the representative FTR signal of 100nm dehydrogenated PECVD a-Si films irradiated upon long pulse laser irradiation within the partial melting regime. For this series, the most prominent and easily

recognized feature is the early and sharp signal oscillation taking place at all incident energy densities (before any substantial melting of the films take place). This behavior indicates that explosive crystallization was promptly triggered as soon as the liquid layer was formed at the film surface [1, 16, 32]. The measured times of the initial peak of the signals are plotted against laser energy density in Figure 6.3. These times were found to be within 145 ± 20ns over the entire range in partial melting regime, well before the time at which incident laser reaches its peak (220ns). This result is consistent with the work that indicated that nucleation of c-Si occurs while the interface of l-Si/a-Si is moving [70] in the course of studying explosive crystallization of ion-implantation amorphized a-Si layer initiated by "long pulse width" (> 45ns FWHM, 532 nm) laser beams (prior to this work, it was thought that crystal solidification was initiated when the interface reached a stationary status (i.e., when it stopped moving).

The early and rapid oscillation signal in FTR essentially implies that as soon as a-Si melts, prompt nucleation of c-Si takes place at the moving l-Si/a-Si interface. The situation is interesting because (1) this behavior is distinct from what was observed with the same films when they were irradiated with short-duration pulses in Section 4.3.2, and (2) the trend is very similar to what was observed previously in microcrystalline-cluster-

rich LPCVD a-Si films (i.e., different samples) when the samples were irradiated with short-duration pulses (Figure 2.7 (a)). While early and prompt explosive crystallization occurring in LPCVD a-Si films has been identified and substantiated to be triggered by preexisting microcrystalline Si clusters embedded within the a-Si matrix [1, 16, 32], explosive crystallization in dehydrogenated PECVD a-Si films must be triggered by actual heterogeneous nucleation of c-Si occurring at the freshly formed and melting l-Si/a-Si interface. Such prompt nucleation and growth will naturally lead to the steep drop following the initial oscillation peak of FTR signal, as the explosive crystallization process proceeds quickly and primarily in the vertical direction. Following the explosive crystallization oscillation, the behavior in the FTR signal can be accounted for in a straight-forward manner by considering primary one-dimensional re-melting and re-solidification of initially explosively crystallized defective/fine-grained Si [16, 32].

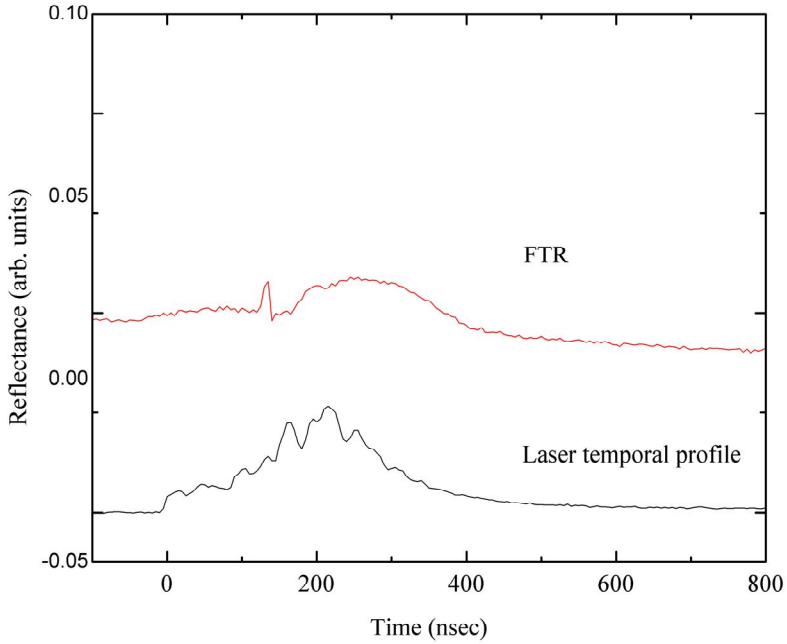

Figure 6.2 Front-side time resolved reflectance (in arbitrary units) at 675nm wavelength of 100nm dehydrogenated PECVD a-Si film on glass substrate as a function of time upon irraidation from a XeCl excimer laser with a long pulse duration (FWHM ~ 240ns) at pulsed laser energy density of 443.2 mJ/cm^2. The complete melting threshold energy density is 561.0 mJ/cm^2.

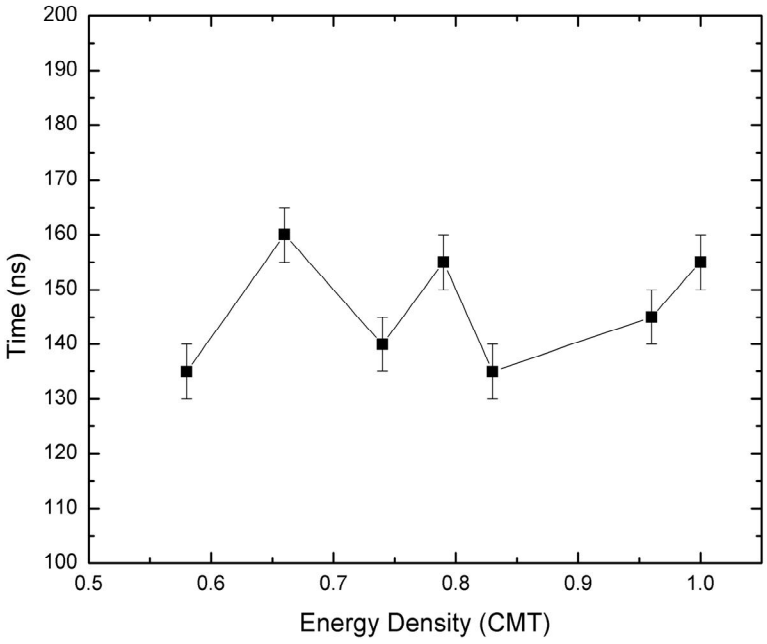

Figure 6.3 Measured times of the initial peak of FTR signals at 675nm wavelength as a function of pulsed laser energy densities for 100nm dehydrogenated PECVD a-Si film on glass substrate upon irradiation with a long pulse duration (FWHM ~ 240ns) laser pulse from a XeCl excimer laser. As shown in Figure 6.2, the laser starts at -4ns and reaches its peak at 220ns. The energy density is calibrated by complete melting threshold (CMT) which is 561.0 mJ/cm^2 for this set of experiments.

6.3.2 Microstructure Analysis

Figure 6.2 shows the planar view TEM micrographs of 100nm dehydrogenated PECVD a-Si films following long pulse excimer laser irradiation at various energy densities in the partial melting regime.

At low energy densities just above the surface melting threshold, the film surface is covered by fine-grained polycrystalline Si. As the energy density increases the grain size gradually increases (as has been also observed by Fogarassy *et al* [80]). This microstructural trend is (as also is the case with the FTR signals) strikingly and apparently similar to short-duration pulse irradiation LPCVD a-Si films, and distinct from what was observed with these PECVD films using short-duration pulses. In particular, the lack of any discernable DSRs within the films was remarkable. Nevertheless, the FTR signals clearly suggest that the overall melting and solidification scenario consists of (1) prompt nucleation of solids that immediately initiates explosive crystallization, and (2) primarily one dimensional re-melting of initially explosively crystallized defective/fine-grained Si at higher energy densities (that, in turn, leads to the formation of gradually larger grains) [1, 16, 32]. Such a trend is expected from considering the enhanced occlusion of grains during upward/vertical solidification as the melt depth increases at higher energy densities.

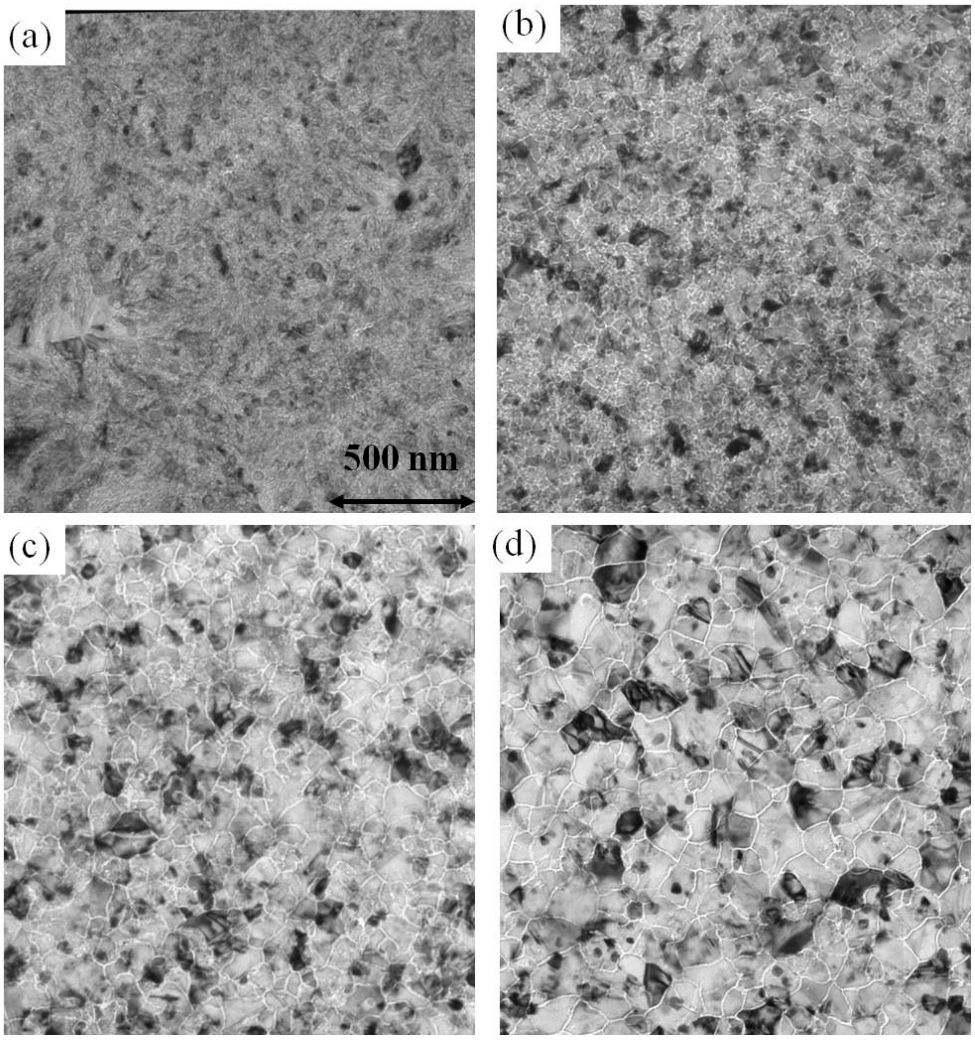

Figure 6.4 Planar view TEM images of 100nm dehydrogenated PECVD a-Si films upon long pulse irradiation at various energy densities: (a) 258.1 mJ/cm^2, (b) 325.4 mJ/cm^2, (c) 375.9 mJ/cm^2, (d) 448.8 mJ/cm^2. Complete melting threshold is 561.0 mJ/cm^2. Secco-etchant was used to enhance the surface grain boundary contrast.

6.4 Discussion

6.4.1 Prompt Nucleation Induced by Long Pulse Duration

As has been observed in Section 4.3.1, the oscillation behavior in the FTR signals suggests that, as soon as a-Si melts at the surface and over the entire partial-melting energy-density range, immediate and prompt solid nucleation takes place at the moving l-Si/a-Si interface. However, this was not observed with the identical films in the case of short-duration pulses (where direct melting of a-Si without any prompt nucleation was the established experimental fact). Since we can eliminate the microcrystals as being the explosive crystallization agents, we inevitably arrive at the conclusion that the necessary condition for promptly triggering nucleation of solids (as the films started to melt at the surface) was realized with the long-duration pulses, but not with the short-duration pulses.

When viewed in terms of one firmly established characteristic regarding the hyper-sensitive nature of the rate of nucleation as a function of undercooling, we feel that the observation reflects what can easily be concluded about the rate of heterogeneous nucleation in the slowly melting interface (clearly expected with long-duration pulses) vs. more

rapidly melting interface (expected with shorter-duration pulses). That is, the greater level of undercooling for heterogeneous nucleation of c-Si at the slowly moving interface does necessarily mean significantly higher nucleation rate, sufficient to induce prompt nucleation of solids. On the other hand, the degree of interfacial undercooling is sufficiently (and at least initially) small enough that nucleation is not observed upon initial melt formation with the short-duration pulses. Only when the rate of nucleation at the interface becomes sufficiently large (due either to increase in undercooling as the interface slows down or to increases in interface roughness at the micro/nano-scale as the interface travels), does the nucleation of solids start at the interface with the short-duration pulses. (More details would be provided via numerical analysis in Chapter 7.)

6.5 Summary

In this chapter, we have investigated a long-duration pulse induced melting and solidification dynamics encountered in dehydrogenated PECVD a-Si films. The results, which are consistent with some of the observations made by other investigators in the field [70, 80], are remarkable in that they are strikingly different from what we observe

with the same samples using short-duration pulses. They are apparently similar (both TEM micrographs and FTR signals) to different samples with different precursor (i.e., LPCVD a-Si films with pre-existing microcrystals) that were irradiated with short-duration pulses. Specifically, the DSRs are remarkably absent in the final microstructure and the FTR signals indicate that early and prompt explosive crystallization when the beam energy is high enough to heat the materials above its melting point (triggered by prompt nucleation converts the film surface into defective/fine-grained Si) is followed with a simple one-dimensional vertical melting and re-growth of the fine-grained material formed initially by explosive crystallization, leading to progressively larger grains at increasing incident laser energy densities.

These results lead us to confirm that the rate of heterogeneous nucleation at the melting interface is, not surprisingly, very strongly dictated by the degree of undercooling, which is affected in a simple and straightforward manner by the duration of the laser pulse.

Chapter 7 Numerical Analysis of Simple Melting and Solidification

7.1 Introduction

As previously described in section 3.5, 3DNS is a numerical program designed and developed to model the rapid melting and solidification of elemental systems on a nanosecond time scale. In this chapter, we employ the 3DNS program to analyze the transformation-related details quantitatively. Through this exercise, we extract some of the parameters and details that are crucial for understanding heterogeneous nucleation occurring at the moving interface of l-Si/a-Si in the present experiments.

When examined in combination with our experimental results, the simulation results assist us to construct an argument with profound implications; the way in which heterogeneous nucleation of c-Si is manifested at the melting front cannot be suitably described by the standard classical-nucleation-theory-based [17] heterogeneous-nucleation expression that assumes a constant solid wetting angle.

From our previous analysis of the transient reflectance signals (Section 4.3.2, 5.3.2 and 6.3.1), we have discussed how it is possible to obtain the temporal information regarding nucleation and re-melting/re-solidification of solids. By comparing what can be easily calculated and simulated using our program in which we intentionally and explicitly do not incorporate c-Si participating in the process (i.e., we simulate simple melting and solidification of a-Si only), we argue that important trends observed experimentally can be quantitatively interpreted to yield information that permits us to make statements about the validity of using standard expression for describing heterogeneous nucleation. This chapter starts by describing the details of simulation, followed by results and discussions in section 7.3. The observations and conclusions will then be summarized in section 7.4.

7.2 Simulation Method

As we concluded in Section 4.4.1, upon laser irradiation above the surface melting threshold, a-Si film can be directly melted, producing a surface layer of l-Si, which is substantially undercooled with respect to the melting point of crystal Si (as a consequence of lower melting temperature of a-Si).

The 3DNS program (Section 3.5, [41]) can be operated to simulate one dimensional melting and solidification of a-Si. The reason for operating in this mode is that, at least the initial part of the transition involves a simple one dimensional situation; uniform "flood" irradiation of microstructurally uniform amorphous Si film, leading to uniform one dimensional heating and subsequent liquid layer formation and growth (i.e., melting). This also means that as soon as nucleation is initiated, one-dimensional description no longer is applicable. However, this does mean that, up to the point at which nucleation is initiated, a one-dimensional exercise is a viable and useful tool in that it does capture all of the complications (such as the temporal shape of the beam, temperature dependent optical and thermal properties, etc.), and provide quantitative information about some key thermal and kinetic details (i.e., evolution in the interfacial temperature, interface velocity, and melt depth) which can be utilized to pinpoint the moment when nucleation takes place. That is to say, these simulated results, when combined with the previously measured time for nucleation (Section 4.3.2, 5.3.2 and 6.3.1), can permit us to estimate the effective temperature at which nucleation is taking place at the l-Si/a-Si interface.

We would like to note that the aim of this one-dimensional simulation exercise is not to simulate the complicated melting and solidification

dynamics we have presented before, but is to use "unrealistic" simulation (which is valid at least up to the point at which nucleation initiates) in which amorphous Si simply melts and resolidifies (without any c-Si participation) in order to obtain a better understanding of the details related to the solid nucleation observed in experiments. This is an indirect, yet effective, way for us to quantitatively analyze the thermal and kinetic situations relevant to the moments when solid nucleation transpires.

The laser pulse profiles recorded by digital oscilloscope in previous experiments (Figure 4.1, 5.1 and 6.1) are used as input to simulate one dimensional melting and solidification of 100nm a-Si films on glass substrates upon laser irradiation with corresponding pulse profiles.

To better compare the simulation results with our previous experimental results, we use the complete melting threshold (CMT) energy density when the Si film undergoes melting throughout the film thickness, as a convenient unit to normalize the energy densities. In our work, a linearized form of the a-Si interface response function (Figure 7.1) is used, as the results are similar to those obtained by using the standard interface response function under low to medium undercooling conditions (~less than 400 K) [83].

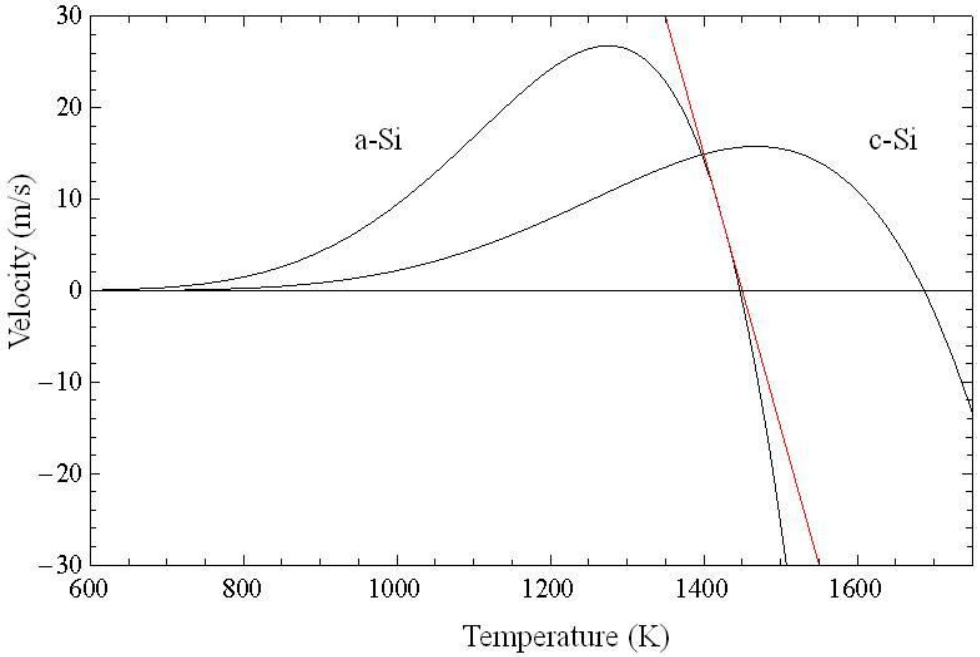

Figure 7.1 Interface response functions used in 3DNS [83] to simulate transformation details in partial melting of a-Si. The linearized form (red) for a-Si is taken as 29.9 cm/(sec K) for melting and solidification.

7.3 Results and Discussion

7.3.1 Applicability of Simplified Classical Nucleation Theory

As concluded in the previous chapters, heterogeneous nucleation of c-Si takes place at the moving l-Si/a-Si interface during the melting process.

Figures 7.2, 7.3, and 7.4 show the simulated results of melt-depth, interface velocity and interface temperature respectively, as a function of time at various incident energy densities corresponding to Figure 4.7.

Referring to Figure 4.7, we observed that the estimated maximum time required for optically observable nucleation events decreases from ~17ns (27ns from the start of laser) to ~10ns (20ns from the start of laser) as the energy density increases from 92.7 mJ/cm^2 (0.34 CMT) to 223.4 mJ/cm^2 (0.82 CMT). By comparing these times to the results shown in Figure 7.2, we can identify that the melt-depth at which "optically significant" degree of solidification via nucleation and growth takes place increases from ~26nm to ~52nm.

Figure 7.3 shows the simulated interface velocity of l-Si/a-Si interface. The simulated melt-velocity reaches its peak value at the time the laser

intensity reaches its peak value (18.4ns), and reaches the zero value (i.e, becomes momentarily stationary) between 30 and 35ns. At a higher energy density, the onset time associated with nucleation is pushed forward towards the time when the melting front is moving faster. This observation leads us to conclude that the moment at which initial nucleation takes place at the melting interface of l-Si/a-Si, while proceeding at deeper melt-depth as the energy density increases, the interfacial melting velocity at the moment of nucleation (which also corresponds to increasing interfacial temperature as shown in Figure 7.4) increases at increasing energy densities.

To summarize, when one examines the simulation results associated with the melting interface from Figure 7.3 and 7.4, and the experimentally measured times associated with the moments at which nucleation takes place in Figure 4.7: one can conclude that nucleation tends to occur, as the energy density increases, at a deeper and more rapidly melting interface, and, therefore, actually at higher interface temperatures.

However, this observation is entirely inconsistent with what can be expected kinetically; a simple heterogeneous nucleation expression, from classical nucleation theory, that relates the rate of heterogeneous nucleation to the degree of supercooling predicts the exact opposite trend.

As we have discussed earlier in Section 2.2, the classical nucleation theory based formulation of heterogeneous nucleation (equation (2.6)) introduces a contact-angle function, f(θ), to account for a reduction in the thermodynamic free-energy barrier associated with the formation of critical clusters. Using the notation of Christian [17], the contact-angle function can be described as follows:

$$f(\theta) = [2 - 3\cos\theta^{l(a)\to c} + (\cos\theta^{l(a)\to c})^3]/4\,, \tag{7.1}$$

where the contact angle factor is $\cos\theta^{l(a)\to c} = (\sigma_{la} - \sigma_{ca})/\sigma_{lc}$;

σ_{la}, σ_{ca}, σ_{lc} are the energies associated with the l-Si/a-Si, c-Si/a-Si and l-Si/c-Si interfaces, respectively [28].

If we assume that the contact angle associated with heterogeneous nucleation of c-Si at the melting front stays constant; then the expression would have predicted that, as the rate of melting increases as the energy density increases, the moments at which nucleation will take place would increase with increasing energy densities.

Therefore, we conclude, based on comparing the simulated to experimental results (Figure 4.7), that the simplified form of classical nucleation theory, with the assumption of constant contact angle, is not applicable for describing heterogeneous nucleation of c-Si at the moving l-

Si/a-Si interface. Since the expression was not developed in the first place for a dynamic/moving interface, perhaps the situation is not so surprising, and that, with a proper modification, classical nucleation theory may, after all, be a proper expression for capturing the observed rate of nucleation.

To this end, we propose that one physical factor that could resolve the situation corresponds to the interfacial topological roughness, which can develop and worsen as the interface is created and travels (i.e., as melting proceeds). A simple extension of classical nucleation theory dictates that rough interface will be significantly more effective at catalyzing heterogeneous nucleation than a smooth interface, as the critical volume can be substantially reduced by the availability of "crevices". Given that amorphous Si at a nano-scale can be viewed as a heterogeneous/non-uniform material, and that planar interface can develop perturbation and become rough during the growth process, it is not inconceivable that the effective potency of the moving melt front increases as melting proceeds. Such an idea, regarding the possibility of microscopically rough melting interface, was identified as a potentially significant factor for affecting the rate of heterogeneous nucleation of c-Si at the l-Si/a-Si interface by Tsao *et al* [28] (albeit for dealing with a somewhat different phenomenon and, ultimately, what appears to be an incorrect description of the

phenomenon). Nevertheless, the argument regarding the situation is a valid one, and may very well be relevant for explaining what we are observing in the present work.

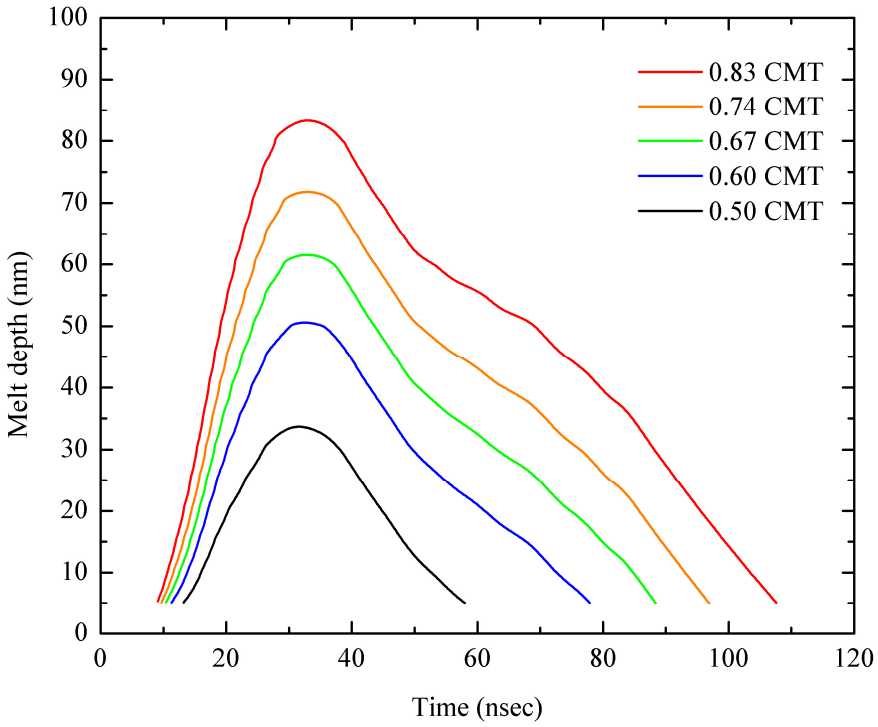

Figure 7.2 Calcuated melt depth vs time upon single peak laser irradiation of 100nm a-Si films on glass substrates at different energy densities. The laser profile is shown in Figure 4.1. Time originates from the start of laser.

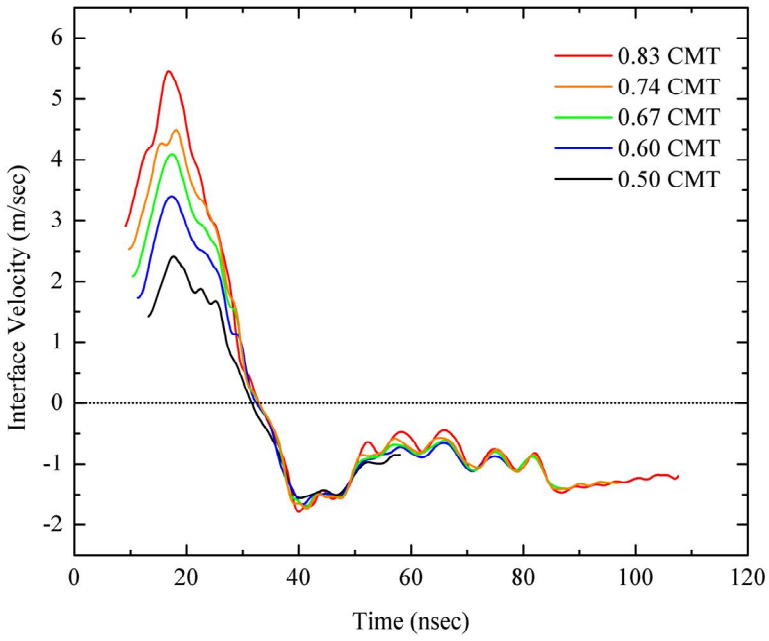

Figure 7.3 Calculated interface velocity evolution of 100nm a-Si films on glass substrates upon single peak laser irradiation at different energy densities. The laser profile is shown in Figure 4.1. Time originates from the start of laser.

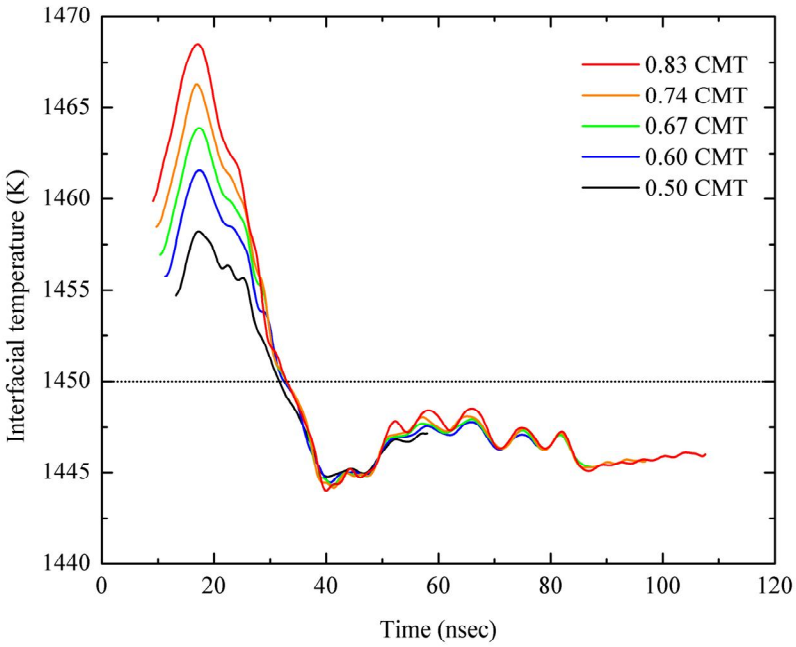

Figure 7.4 Calculated interface temperature evolution of 100nm a-Si films on glass substrates upon single peak laser irradiation at different energy densities. The laser profile is shown in Figure 4.1. Time originates from the start of laser.

7.3.2 Effect of the Second Peak in Laser Pulse Profile

Under excimer laser irradiation with a second peak in the laser profile (Figure 5.1), the FTR signal exhibits a second peak that indicates that a commensurate re-melting of the film is taking place (Section 5.4). (The measured times of the initial peak and dip in FTR were plotted in Figure 5.7.) Figures 7.5, 7.6, and 7.7 show the simulated results of the melt-depth, interface velocity and interface temperature, respectively, as a function of time at various incident energy densities (corresponding to Figure 5.7).

In Figure 5.7, the measured time of the initial peak in FTR signal is found to decrease with increasing energy density. Specifically it drops from 24ns to 16ns (corresponding to ~28ns to 20ns from the start of the laser pulse) as the energy density increases from 0.53 CMT to 0.94 CMT. Combining with the simulation results from Figure 7.5, the measured time indicates that, as the incident energy density increases, nucleation occurs, not surprisingly, at a larger melt depth. Similarly, the simulated interface velocity and temperature evolution in Figure 7.6 and 7.7 also implies that at a higher energy density, nucleation tends to occur at a higher interface velocity (and thus a higher interface temperature/lower degree of supercooling). This confirms the observation in single peak laser irradiation, and could also be accounted for in a similar way as discussed in the previous section.

Figure 5.7 also shows that the dip observed in FTR signal stays remarkably constant at 41ns (~45ns from the start of laser) over the entire energy density range; indicative of the re-melting process as a result of the second peak in the laser profile. Since re-melting occurs after the onset of nucleation, our simple one-dimensional model, in which solidification proceed only via re-growth of a-Si (i.e., no nucleation of c-Si) is not appropriate to account for solidification and possible re-melting that ensue the nucleation of solids.

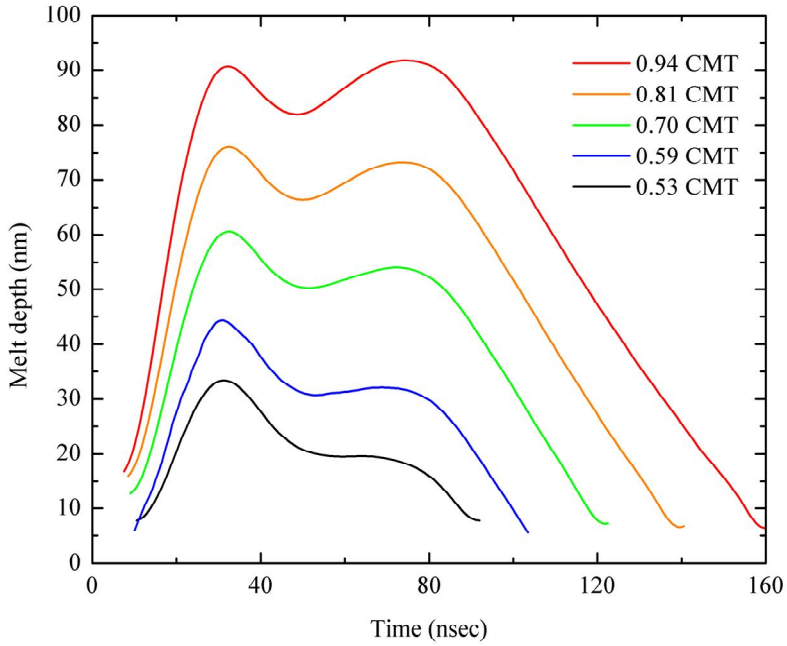

Figure 7.5 Calcuated melt depth vs time upon double peak laser irradiation of 100nm a-Si films on glass substrates at different energy densities. The laser profile is shown in Figure 5.1. Time originates from the start of laser.

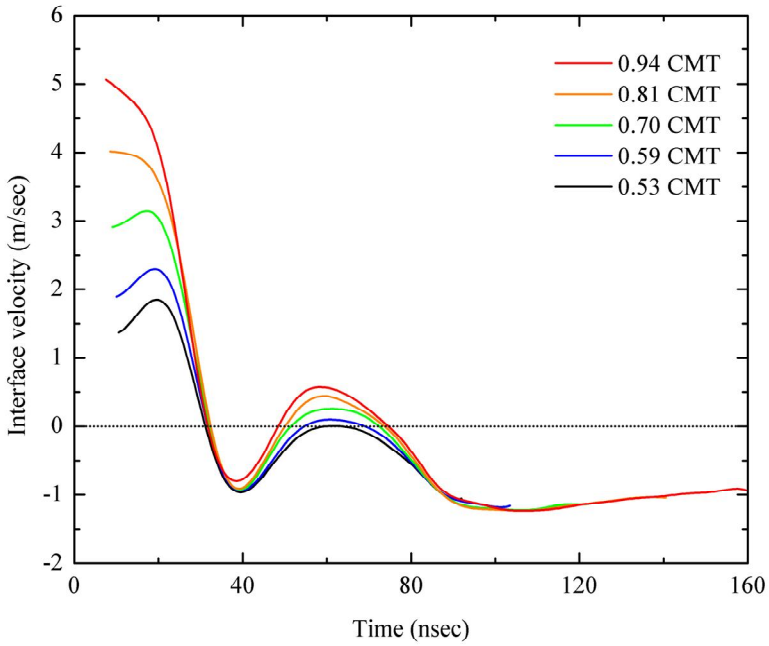

Figure 7.6 Calculated interface velocity evolution of 100nm a-Si films on glass substrates upon double peak laser irradiation at different energy densities. The laser profile is shown in Figure 5.1. Time originates from the start of laser.

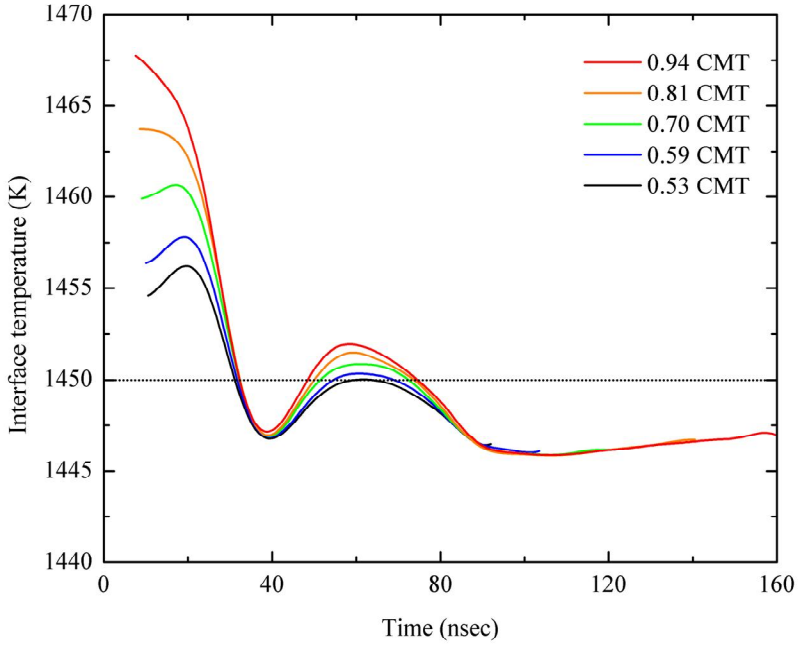

Figure 7.7 Calculated interface temperature evolution of 100nm a-Si films on glass substrates upon double peak laser irradiation at different energy densities. The laser profile is shown in Figure 5.1. Time originates from the start of laser. .

7.3.3 Effect of Laser Pulse Duration

The most notable and dominant effect associated with the long-duration-pulse induced behaviour was that nucleation was found to take place as soon as melting was induced at the surface (Section 6.4.2). Figures 7.8, 7.9, and 7.10 show the simulated results of melt-depth, interface velocity and interface temperature as a function of time at various incident energy densities in the partial melting regime for the case in which a-Si film was irradiated with the exact temporal profile utilized in the long-pulse-duration experiments.

The experimentally measured times of the initial peak of FTR signals (as shown in Figure 6.3) stay in the range of 130 and 160ns. The simulated results in Figure 7.8 show that these times correspond to the moments prior to the point when the melt reaches its maximum depth (around 300ns). Once again, this result is consistent with the points discussed in Chapter 6, and supports the notion that prompt and early nucleation occurs over the entire energy densities.

It is also shown in Figures 7.9 and 7.10 that the interface moves very slow even at high energy densities close to CMT, and the interface temperature always stays close to the melting point of a-Si (1450 K). This result, which is entirely consistent with what can be thermally and kinetically expected

from the situation, does quantitatively validate the idea that the prompt nucleation taking place upon the film being melted is entirely kinetically consistent (since the degree of supercooling at the interface is the largest, as was discussed in Section 6.4).

Also relevant is the actual shape of the long-pulse duration profile. As a consequence of the way in which the beam is split up, delayed and put together, the profile contains a number of peaks and valleys. This in turn will lead to corresponding fluctuations in the interface velocity; at local minimum points, one can thus expect substantially increased chance of nucleation (due to greater supercooling associated with such points). This strong oscillation behaviour can be seen in both Figures 7.9 and 7.10, resulting from the corresponding oscillations in the laser profile (Figure 6.1). These results demonstrate how such intensity oscillations in the laser profile must be conducive to triggering explosive crystallization, as consistently observed experimentally by the explosive oscillations in the FTR signals (Figure 6.2).

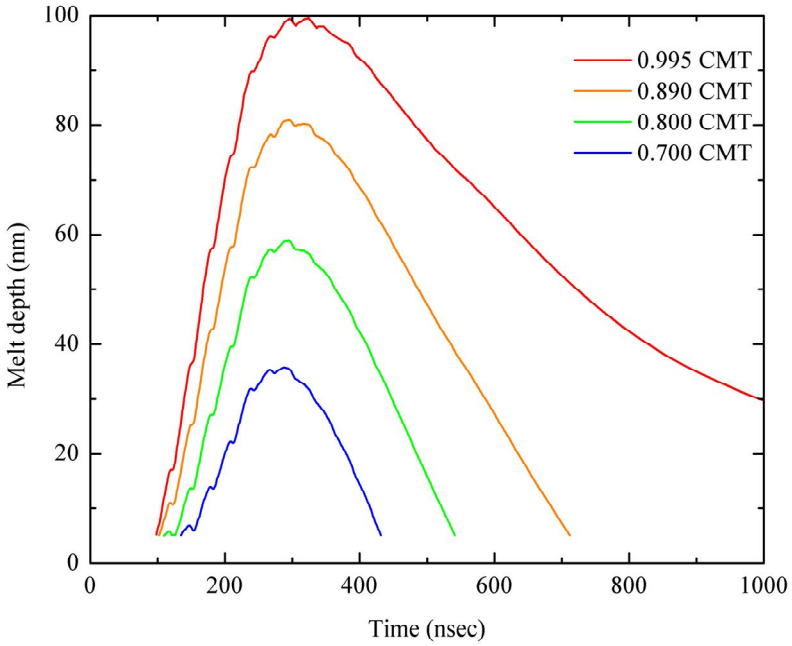

Figure 7.8 Calcuated melt depth vs time upon long pulse duration laser irradiation of 100nm a-Si films on glass substrates at different energy densities. The laser profile is shown in Figure 6.1. Time originates from the start of laser.

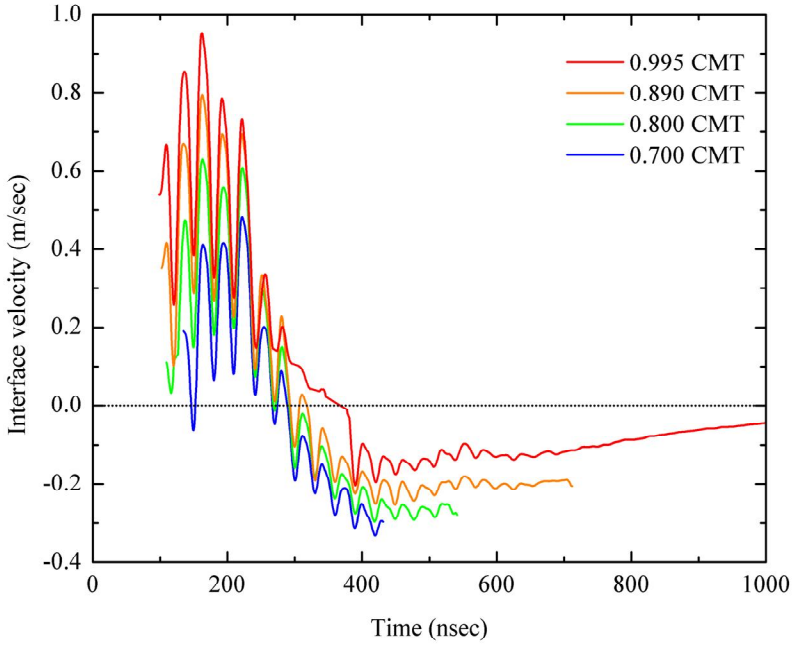

Figure 7.9 Calculated interface velocity evolution of 100nm a-Si films on glass substrates upon long pules duration laser irradiation at different energy densities. The laser profile is shown in Figure 6.1. Time originates from the start of laser.

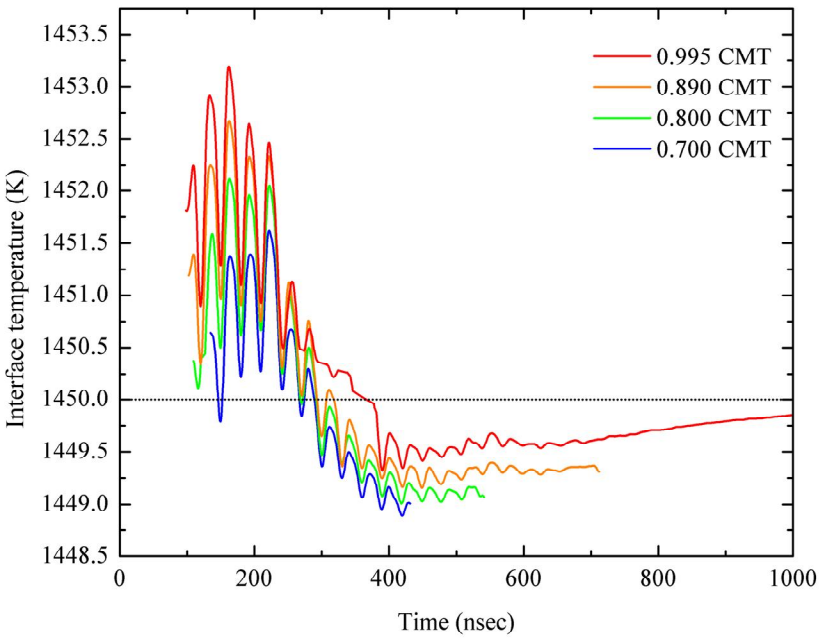

Figure 7.10 Calculated interface temperature evolution of 100nm a-Si films on glass substrates upon long pulse duration laser irradiation at different energy densities. The laser profile is shown in Figure 6.1. Time originates from the start of laser.

7.4 Summary

In this chapter we presented the results obtained by numerically calculating simple one-dimensional melting and solidification of a-Si. The utility of the exercise was that the numerical nature of the calculation permitted us to incorporate various beam profiles and temperature dependent properties while being entirely appropriate up until the point at which nucleation is triggered. Since nucleation corresponds to one of the topics we are interested in this thesis, the numerical results permit us to quantitatively analyze the thermal and kinetic environment associated with heterogeneous nucleation of c-Si, which we have found to initiate solidification for all irradiation scenarios considered in this thesis.

Through such an exercise, we concluded that the nucleation behaviour of c-Si at the moving l-Si/a-Si interface could not be properly accounted for by using a simplified form of classical nucleation theory, which assumes constant contact angle at the planar interface. Furthermore, we suggested that interface roughness may be a critical factor that would enhance the nucleation rate with increasing melt-depth.

Chapter 8 Conclusions

8.1 Summary

This thesis investigates how melting and solidification occurs when a-Si films are irradiated using a high-intensity laser pulse. The details of transitions are scientifically interesting in that the melting of amorphous Si means melting of a metastable phase, which must transpire well below the equilibrium point associated with the stable phase. This, in turn, instantaneously creates a thermodynamically severe environment within which the stable phase can eventually and readily participate via nucleation and growth. Technologically, these melting and solidification details are needed in order to better understand, and eventually optimize, excimer-laser-induced melt-mediated crystallization of dehydrogenated PECVD amorphous Si films being employed in the manufacture of advanced flat-panel displays. (These particular films are also interesting to examine scientifically as they are effectively free of microcrystals that can lead to a

more predictable and straight-forward melting and solidification scenario within which no spontaneous nucleation participates.)

The experimental approach combining *in situ* transient reflectance measurements and post-irradiation microstructural analysis were employed to untangle unusual and complex transitional sequences. The most significant experimental results were obtained by using a simple "short duration" Gaussian-temporal profiled pulse. The findings presented us with an opportunity to decipher a number of previously unresolved and misinterpreted details regarding the transitions. The most important microstructural feature observed in the irradiated films corresponds to circular regions, referred to as disk-shaped regions (DSRs), which typically consist of defective core areas and, to a varying degree, less defective outer perimeters.

Based on this and other microstructural findings and corresponding transient reflectance signals, we suggested a model consisting of the following elements: (1) solidification is initiated (in these microcrystalline-cluster-free a-Si films) by heterogeneous nucleation of crystal Si occurring at the moving interface between liquid and amorphous (during the amorphous Si melting phase), (2) subsequent solidification following nucleation proceeds, at least initially, to generate extremely defective fine-grained Si via the defective mode of crystal growth, and (3) spatially localized preferential

re-melting and re-solidification of defective regions and grain boundaries can take place, surprisingly, while the beam is still on.

The above model presented in this thesis is distinct from a number of arguments and models that were previously suggested by other investigators in dealing with the research topics that are related to the present thesis. Our model, we argue, is the only model which is consistent with all experimental results that have been obtained (by us as well as others). It also addresses some of the important questions and details associated with the initiation and propagation of explosive crystallization (Section 2.3.1).

We have also investigated the effects arising as a result irradiating a-Si films using a "double-peak" temporal-profiled pulse and a "long-pulse-duration" profile. These situations presented both microstructural and transient reflectance results that were, while apparently different from those obtained using a single-peak profile, consistently explained using the above model by considering the expected thermal and kinetic changes that are introduced as a consequence of using the modified beam profiles. Specifically, the dual-peak profile leads to enhanced re-melting of the solid during the transitions, as a consequence of the energy deposition from the second peak. The long-duration profile leads to very prompt triggering of the explosive crystallization (as a consequence of the "slower" melting front being more

severely undercooled) eventually followed by a relatively simple vertical melting and re-solidification of the explosively crystallized/fine-grained Si layer.

We have also performed a simple quantitative analysis using a one-dimensional simulation method that does not try to mimic what actually takes place experimentally. Instead it simulates an extremely simple scenario consisting of direct melting and re-solidification/amorphization of the amorphous layers (without any participation of the equilibrium c-Si phase). By comparing the results from the simulation to what we actually observe experimentally, we were able to conclude that the simple form of classical nucleation theory, which treats heterogeneous nucleation by assuming constant contact angle at the interface, may not be applicable to the situation encountered in these experiments.

Finally, we have briefly discussed the implications of these findings on the conventional ELA method and the possibility of developing a new ultra-high-through put laser crystallization method.

8.2 Suggestions for future work

The present work addresses the melting and solidification dynamics of a-Si upon being single-shot excimer-laser irradiated. Given that the established

ELA method requires multiple shots to produce a satisfactory final microstructure for making high-performance TFTs, a more in-depth study of the multi-shot process can only be useful in optimizing the ELA method (by reducing the number of shots and thus increasing the throughput).

Another direction for future work could involve the development of a theoretical approach incorporating the interfacial roughness effect into the classical nucleation theory to describe the heterogeneous nucleation encountered in this thesis. However, since the classical nucleation theory for condensed systems has never been quantitatively and rigorously tested (one can strongly argue) by experimental results so far, making the modifications (to the theory to qualitatively describe heterogeneous nucleation of solids proceeding at the melting front) may be viewed as being less than a fully compelling exercise.

It is also worth noting that in this work, we utilized laser pulses with the pulse durations between 30ns and 240ns. Investigation of the partial melting behavior under even longer pulse durations may provide us with additional information on the triggering and sustaining mechanisms of solidification, since, eventually, solid phase crystallization could participate under appropriately moderate heating rates [84]. As well, conducting experiments using shorter pulses should also be worthwhile. Doing so will create even

more severe thermal and kinetic environment within which melting and solidification transitions will proceed.

Appendix A Pulsed Laser-induced Partial Melting of BHF-etched PECVD a-Si Films in Vacuum

A. 1. Introduction

A recent investigation [83] dealing with the nucleation mechanism in supercooled liquid Si films on SiO_2 substrates has shown that under certain conditions, the presence of native/surface oxide on the melted films can induce heterogeneous nucleation of laser quenched and completely melted Si films. In particular, the work has shown that it was possible to eliminate such heterogeneous nucleation taking place at the "top interface" by implementing the following additional experimental procedures: (1) before being irradiated, buffered hydrofluoric acid (BHF) etchant should remove the surface native oxide layer, and (2) the samples should be irradiated in a vacuum chamber.

In order to examine the possibility of solid heterogeneous nucleation taking place at the top surface of the partially melted amorphous Si films (which is theoretically possible as the liquid layer is substantially supercooled with respect to the crystal phase), we examine what happens when pre-BHF-

etched PECVD a-Si films are irradiated in a vacuum ambient. By comparing the findings with those obtained in Chapter 5 under air irradiation conditions, we conclude that no such heterogeneous nucleation takes place at the surface of the partially melted amorphous Si films.

A. 2. Experimental Details

Experiments were conducted using the XeCl excimer laser system. The temporal profile of the irradiation laser pulse is shown in Figure 5.1. The experimental setup for the transient reflectance measurements was similar to that employed in Chapter 5. The surface of the sample was etched by BHF solution prior to being irradiated in a vacuum chamber (as described in [83]), and the pressure of the chamber stayed within the range of 10^{-5} to 10^{-1} Torr in the laser irradiation experiments.

A. 3. Results and Discussion

Figure A.1 shows both the FTR and BTR signals of a-Si films irradiated in vacuum. Extracted from FTR signals in Figure A.1, the "initial peak" time (as explained in Section 5.3.2) in Figure A.2 provides the information on the time when initial nucleation takes place. The trend observed from the data

(where the initial nucleation time decreases with increasing incident energy density) is essentially consistent with what was observed as presented in the chapter 5 of this thesis (Figure 5.7). Furthermore, these measured times are similar to those in Figure 5.7 at corresponding energy densities. In other words, we did not observe any change in nucleation time (Figure 5.6 and 5.7).

As for the nature of the nucleation occurring under the condition of a "clean" sample surface and vacuum ambient (therefore, the top liquid is a free surface during the melting of a-Si), the possibility of nucleation occurring at the top liquid surface can be safely discounted from thermodynamic considerations. (As shown in Figure 2.3, the nucleus could not form on the free surface where only the interfacial energy of the l-Si/c-Si exists.) It can thus be concluded from the exercise conducted in this appendix that the physical arguments we have provided in the main body of this thesis stand as being consistent and valid.

A. 4. Summary

In this appendix, we employed several experimental procedures implemented in a recent paper [83] to examine the possibility of solid heterogeneous nucleation taking place at the top native-oxide/liquid Si

interface. Based on the observations, we identify that the air ambient and the native oxide layer on the sample surface do not affect the nucleation mechanism involved in partial melting of amorphous Si films.

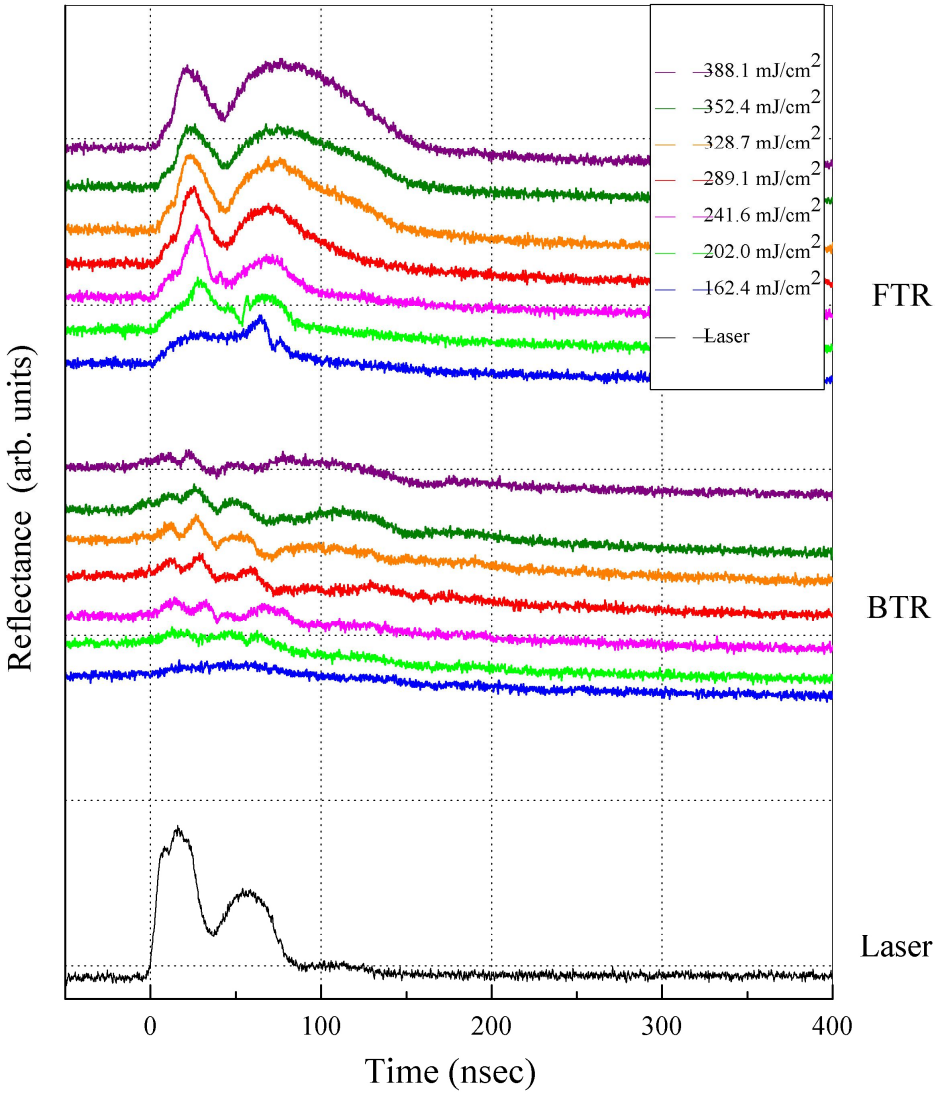

Figure A. 1 Front-side and back-side time resolved reflectance (in arbitrary units) at 675nm wavelength of 100nm dehydrogenated PECVD a-Si film on glass substrate irradiated in vacuum with the native oxide removed by BHF solution prior to irradiation. The double-peak laser pulse from a XeCl excimer laser starts at -4ns and reaches the first peak at 15ns, the first minimum at 34ns, and the second peak at 54ns. Complete melting threshold is 396.0 mJ/cm².

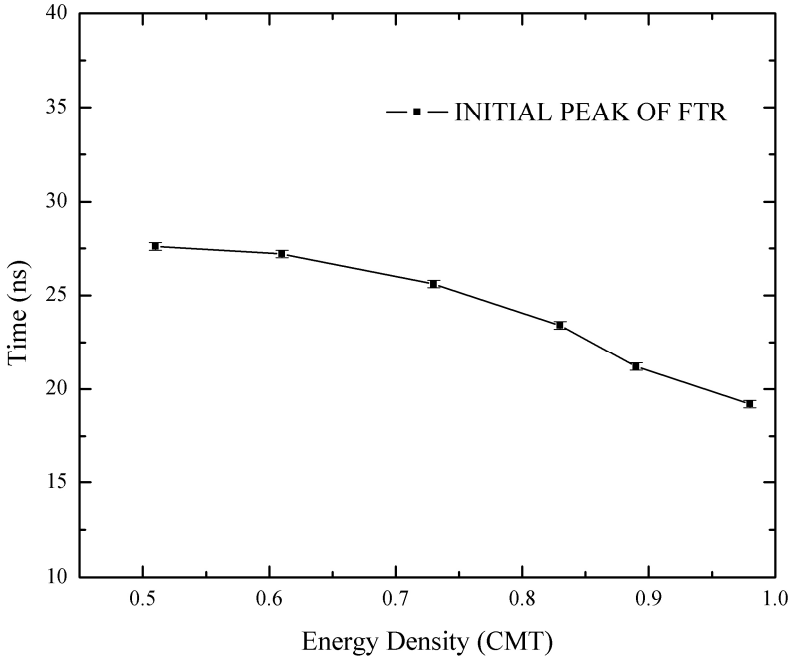

Figure A. 2 Measured times of the initial peak of front-side time resolved reflectance (as presented in Figure A.1) at 675nm wavelength as a function of pulsed laser energy densities for 100nm dehydrogenated PECVD a-Si film on glass substrate irradiated in vacuum with the native oxide removed by BHF solution prior to irradiation. As shown in Figure A.1, the double-peak laser pulse starts at -4ns and reaches the first peak at 15ns, the first minumum at 34ns, and the second peak at 54ns. The energy density is calibrated by complete melting threshold (CMT) which is 396.0 mJ/cm^2 for this set of experiments.

Appendix B Pulsed Laser Crystallization of Solid-phase Crystallized and SOI Si Films

B. 1. Introduction

In this appendix, we examine what can be construed as being a very simple case of partial melting crystalline Si films. One motivation for doing this is to prepare for investigating the multiple-shot-induced "grain growth" effect observed in ELA (excimer laser annealing) of Si films. Here, we deal with less challenging situations involving partial melting of solid-phase crystallized Si films (large-grained polycrystalline material with high density of intragrain defects) and single crystal SOI films. This exercise points out that it is important to be aware of the change in the reflectance of the solid films caused by the temperature change during the pre-melting portion of the process. When this effect was taken into account in interpreting the transient reflectance data, it was possible to conclude that, as expected, a

simple partial melting and solidification scenario involving vertical melting and solidification of the films transpired upon being irradiated.

B. 2. TR analysis of polycrystalline-Si films

The experimental setup used for time-resolved transient reflectance measurements is illustrated in Chapter 4. The samples consisted of 100-nm-thick LPCVD a-Si films deposited on SiO_2-coated quartz substrates. These films were then fully transformed into polycrystalline-Si films via solid-phase crystallization at 700^{o}C for two hours.

Figure B.1 presents both the front-side and back-side time-resolved reflectance of 100nm polycrystalline-Si films upon being irradiated at various energy densities. It is evident that both the initial increase in the front-side signal and the initial decrease in the back-side signal occurred prior to primary melting of the poly-crystalline Si. This could be explained by taking into consideration the interference effect resulting from the change in optical properties of poly-crystalline Si upon preheating the film. Calculations of front-side and back-side reflectance (Figure B.2 (a) and B.3 (a)) based on interference model [61, 62] are also in good agreement with the observed behavior. As the surface melts, the observed increase in FTR and oscillations in BTR signals are in accordance with thin film interference

model calculation [16, 32], assuming a simple melting and vertical growth model (Figure B.2 (b) and B.3 (b)).

These observations suggest that partial melting of solid-phase crystallized polycrystalline Si follows the simple one-dimensional vertical melting and solidification scenario. This is not surprising, given that both the flat surface and the large-grained polycrystalline Si microstructure (with high density of intra-grain defect) in solid-phase crystallized film suggest the vertical planar motion of l-Si/c-Si interface during transformation. In contrast, the polycrystalline Si films obtained from ELA consist of small clean grains with protrusions on the surface, and a proper interpretation of how these films are melted and solidified in the ELA method (where some degree of localized complete melting can be argued as being necessary) is expected to involve more a sophisticated treatment of melting details.

B. 3. TR analysis of Silicon on Insulator (SOI) wafer

This section describes partial melting irradiation of single crystal Si film, which corresponds to the simplest case from the viewpoints involving thermal and phase transformation considerations.

The samples used here are 190nm <111> Si on SOI wafer with 376nm silicon oxide buffer layer and the experimental setup is similar to that employed in

Chapter 4, except that only front-side transient reflectance signals are captured as the SOI wafer did not permit us to conduct the back-side analysis.

Figure B.4 shows the FTR signal at 650nm for single crystal Si film single-shot irradiated at various laser pulse energy densities. As expected, the FTR signal increases to a peak value as the surface melts. Moreover, a prominent initial peak is observed before Si surface melting. This observation is in good agreement with the calculation results (as shown in Figure B.5 (a)) based on the interference model, considering the temperature effect on optical properties of both c-Si and silicon oxide. This also demonstrates how the interference effect could significantly alter the value of thin film reflectance as a function of the film temperature.

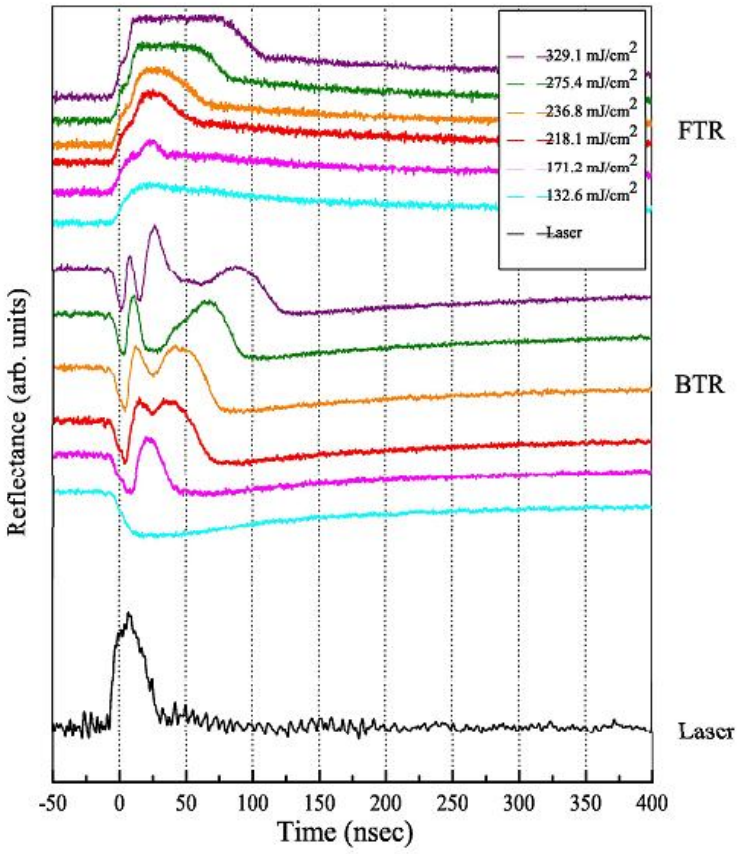

Figure B. 1 Front-side and back-side transient reflectance (in arbitray units) at 650nm and 790nm wavelength respectively of 100nm polycrystalline-Si films on quartz substrate as a function of time and laser energy densities upon irradiation with a ~30ns FWHM pulse from a XeCl excimer laser. Complete melting threshold is 361.0 mJ/cm^2.

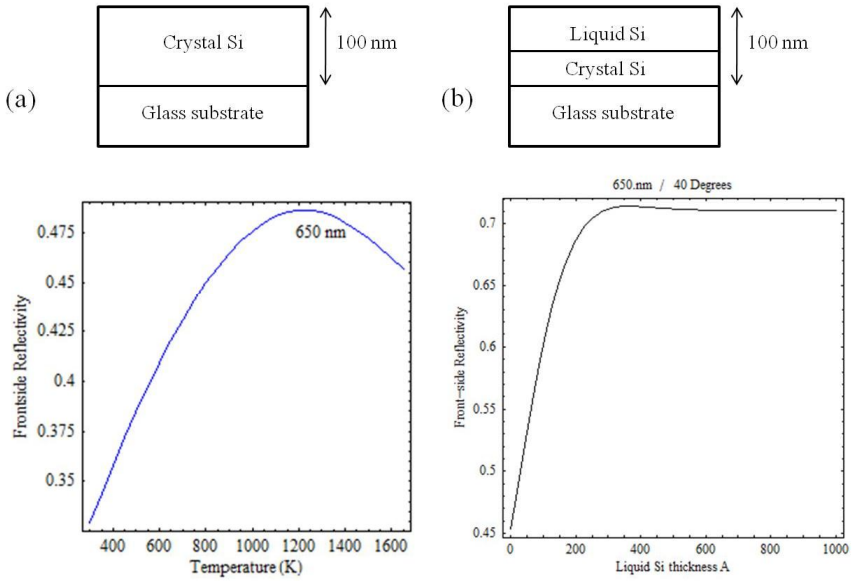

Figure B. 2 Calculation of front-side reflectance based on thin film interference multilayer reflectance analysis. (a) Multilayered structure of 100nm c-Si thin film on glass sustrate and calculated front-side reflectance as a function of temperature. (b) Multilayered structure of 100nm c-Si thin film on glass substrate that undergoes simple one dimensional vertical melting and solidification process and front-side reflectance as a function of liquid Si thickness on top at 650nm wavelength. The optical index values of each material were taken from references [2-5] at 1650K.

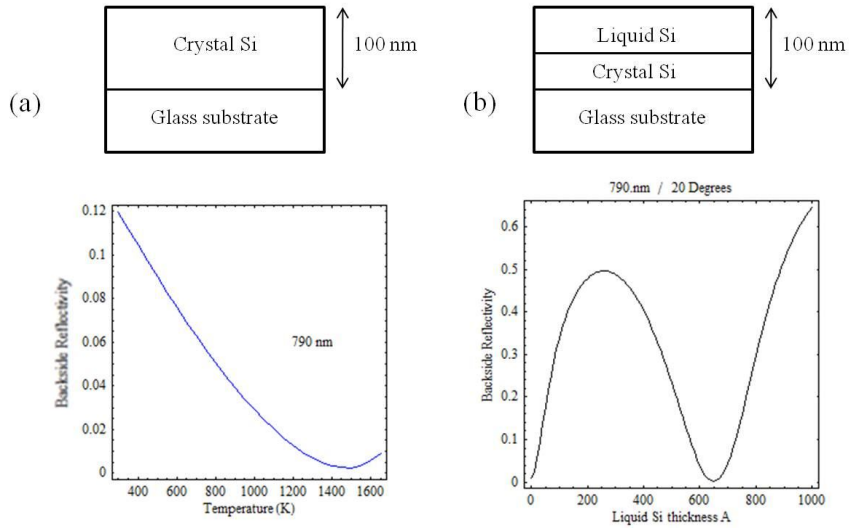

Figure B. 3 Calculation of back-side reflectance based on thin film interference multilayer reflectance analysis. (a) Multilayered structure of 100nm c-Si thin film on glass sustrate and calculated front-side reflectance as a function of temperature. (b) Multilayered structure of 100nm c-Si thin film on glass substrate that undergoes simple one dimensional vertical melting and solidification process and back-side reflectance as a function of liquid Si thickness on top at 790nm wavelength. The optical index values of each material were taken from references [2-5] at 1650K.

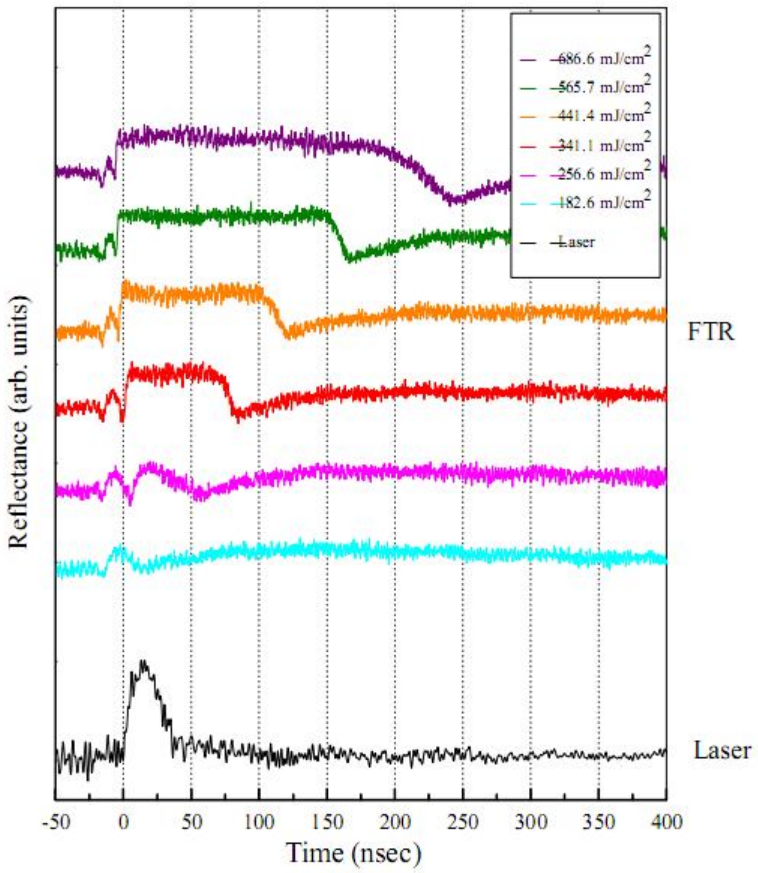

Figure B. 4 Front-side transient reflectance (in arbitray units) at 650nm wavelength of 190nm <111> single crystal Si film on SOI wafer as a function of time and laser energy densities upon irradiation with a ~30ns FWHM pulse from a XeCl excimer laser. Complete melting threshold is 690.0 mJ/cm^2.

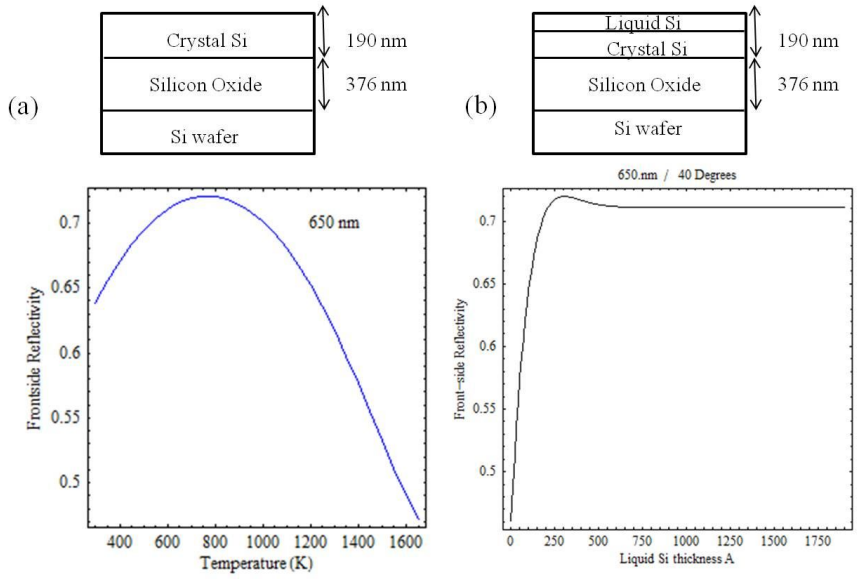

Figure B. 5 Calculation of front-side reflectance based on thin film interference multilayer reflectance analysis. (a) Multilayered structure of 190nm c-Si thin film on Si wafer with 376nm oxide buffer layer and calculated front-side reflectance as a function of temperature. (b) Multilayered structure of 190nm c-Si thin film on SOI wafer that undergoes simple one dimensional vertical melting and solidification process and front-side reflectance as a function of liquid Si thickness on top at 650nm wavelength. The optical index values of each material were taken from references [2-5] at 1650K.

References

1. J.S. Im, H.J. Kim, and M.O. Thompson, Appl. Phys. Lett. **63**, 1969 (1993).
2. J. Sik, J. Hora, and J. Humlicek, J. Appl. Phys. **84**, 6291 (1998).
3. M.A. Green, Solar Energy Materials & Solar Cells **92**, 1305 (2008).
4. G.E. Jellison and F.A. Modine, J. Appl. Phys. **76**, 3758 (1994).
5. G.E. Jellison and F.A. Modine, Appl. Phys. Lett. **41**, 180 (1982).
6. J.W. Hamer, A. Yamamoto, G. Rajeswaran, and S.A. Van Slyke, Digest of Technical papers - SID International Symposium **36**, 1902 (2005).
7. C. Helum, *Properties of Silicon*. Surrey, England: INSPEC. 1988.
8. E.P. Donovan, F. Spaepen, D. Turnbull, J.M. Poate, and D.C. Jacobson, Appl. Phys. Lett. **42**, 698 (1983).
9. K. Murakami, H.C. Gerritsen, H. van Brug, F. Bijkerk, F.W. Saris, and M.J. van der Wiel, Phys. Rev. Lett. **56**, 655 (1986).
10. F. Spaepen and D. Turnbull, AIP Conf. Proc. **50**, 73 (1979).
11. B.G. Bagley and H.S. Chen, ibid., 97.
12. J.M. Poate, Mat. Res. Soc. Symp. Proc. **13**, 263 (1983).
13. P.S. Peercy, M.O. Thompson, and J.Y. Tsao, Mat. Res. Soc. Symp. Proc. **80**, 39 (1987).
14. D.E. Polk and D.S. Boudreaus, Phys. Rev. Lett. **31**, 92 (1973).
15. T.I. Kamins, *Polycrystaline Silicon for Intergrated Circuit Applications*. Boston: Kluwere Academic. 1988.
16. J.H. Yoon, Ph.D. thesis, Columbia University (1998).
17. J.W. Christian, *The Theory of Transformations in Metals and Alloys*. 2nd ed: Pergamon, Oxford. 1975.

18. S. Hazair, Ph. D thesis, Columbia University (2005).

19. G.L. Olson and J.A. Roth, *Materials Science Reports*. Amesterdam. 1988.

20. D. Turnbull, Journal of Physical Chemistry **66**, 609 (1962).

21. B.C. Larson, J. Tischler, and D. Mills, J. Mater. Res. **1**, 144 (1986).

22. G.J. Galvin, J.W. Mayer, and P.S. Peercy, Appl. Phys. Lett. **46**, 644 (1985).

23. P.H. Bucksbaum and J. Bokor, Phys. Rev. Lett. **53**, 182 (1984).

24. P.A. Stolk, A. Polman, and W.C. Sinke, Physical Review B **47**, 5 (1993).

25. M.O. Thompson, G.J. Galvin, M.J. W., P.S. Peercy, J.M. Poate, D.C. Jacobson, A.G. Cullis, and N.G. Chew, Phys. Rev. Lett. **52**, 2360 (1984).

26. G.H. Glimer and H.J. Leamy, *Laser and Electron Beam Processing of Materials*, ed. C.W. White and P.S. Peercy: Academic Press. 1980.

27. D.H. Lowndes, S.J. Pennycook, G.E. Jellison, S.P. Withrow, and D.N. Mashburn, J. Mater. Res. **2**, 648 (1987).

28. J.Y. Tsao and P.S. Peercy, Phys. Rev. Lett. **58**, 2782 (1987).

29. S. Roorda and W.C. Sinke, Appl. Surf. Sci. **36**, 588 (1989).

30. S.D. Brotherton, D.J. McCulloch, J.B. Clegg, and J.P. Gowers, IEEE Trans. Elect. Dev. **40**, 407 (1993).

31. J.S. Im and H.J. Kim, Appl. Phys. Lett. **64**, 2303 (1994).

32. J.H. Yoon and J.S. Im, Metals and Materials **5**, 525 (1999).

33. H.J. Kim, J.S. Im, and M.O. Thompson, Mat. Res. Soc. Symp. Proc. **283**, 703 (1992).

34. F.S. D'Aragona, J. Electrochem. Soc. **119**, 948 (1972).

35. J.P. Leonard and J.S. Im, Mat. Res. Soc. Symp. Proc. **580**, 233 (2000).

36. J.P. Leonard and J.S. Im, Appl. Phys. Lett. **78**, 3454 (2001).

37. M.J. Uttormark, Ph.D thesis, Cornell University (1992).

38. V.V. Gupta, H.J. Song, and J.S. Im, Appl. Phys. Lett. **71**, 99 (1997).

39. D. Turnbull, Solid State Physics **3**, 225 (1956).

40. D. Turnbull, Journal of Applied Physics **21**, 1022 (1950).

41. J.P. Leonard, Ph. D thesis, Columbia University (2000).

42. A. Polman, D.J.W. Mous, P.A. Stolk, W.C. Sinke, C.W.T. Bulle-Lieuwma, and D.E.W. Vandenhoudt, Appl. Phys. Lett. **55**, 1097 (1989).

43. A. Polman, S. Roorda, P.A. Stolk, and W.C. Sinke, Journal of Crystal Growth **108**, 114 (1991).

44. W.C. Sinke, A. Polman, S. Roorda, and P.A. Stolk, Appl. Surf. Sci. **43**, 128 (1989).

45. L. Mariucci, A. Pecora, G. Fortunato, C. Spinella, and C. Bongiorno, Thin Solid Films **427**, 91 (2003).

46. G.E. Jellison and D.H. Lowndes, Appl. Phys. Lett. **51**, 352 (1987).

47. A.G. Cullis, H.C. Webber, and N.G. Chew, Appl. Phys. Lett. **36**, 547 (1980).

48. J. Narayan and C.W. White, Appl. Phys. Lett. **44**, 35 (1984).

49. F.C. Voogt and R. Ishihara, J. Appl. Phys. **95**, 2873 (2004).

50. F.C. Voogt and R. Ishihara, Thin Solid Films **383**, 45 (2001).

51. H.J. Leamy, W.L. Brown, G.K. Celler, G. Foti, G.H. Gilmer, and J.C.C. Fan, Appl. Phys. Lett. **38**, 137 (1981).

52. H.S. Cho, Ph.D. Thesis, Columbia University (2003).

53. H.S. Cho, D. Kim, A.B. Limanov, M.A. Crowder, and J.S. Im, Mat. Res. Soc. Symp. Proc. **621**, Q9.9.1 (2000).

54. S. Hazair, P.C. van der Wilt, Y. Deng, U.-J. Chung, A.B. Limanov, and J.S. Im, Mat. Res. Soc. Symp. Proc. **979**, HH11-22 (2007).

55. M.O. Lampert, J.M. Koebel, and P. Stiffert, J. Appl. Phys. **52**, 4975 (1981).

56. R.F. Wood and G.A. Geist, Phys. Rev. Lett. **57**, 873 (1986).

57. J. Narayan, S.J. Pennycook, D. Fathy, and O.W. Holland, J. Vac. Sci. Technol. A **2**, 1495 (1984).

58. J.J.P. Bruines, R.P.M. van Hal, and H.M.J. Boots, Appl. Phys. Lett. **49**, 1160 (1986).

59. D.H. Lowndes, G.E. Jellison, S.J. Pennycook, S.P. Withrow, and D.N. Mashburn, Appl. Phys. Lett. **48**, 1389 (1986).

60. K. Murakami, O. Eryu, K. Takita, and K. Masuda, Phys. Rev. Lett. **59**, 2203 (1987).

61. D.D. Dunn, J.A. Bruce, and M.S. Hibbs, SPIE Proc. **1463**, 8 (1991).

62. H.A. Macleod, *Think Film Optical Filters*. 2nd ed. New York: Macmillan. 1986, page 11.

63. K. Murakami, K. Takita, and K. Masuda, Jpn.J.Appl.Phys **20**, L867 (1981).

64. T. Eiumchotchawalit and J.S. Im, Mat. Res. Soc. Symp. Proc. **321**, 725 (1994).

65. R.B. Iverson and R. Reif, Journal of Applied Physics **57**, 5169 (1985).

66. M.O. Thompson, J.W. Mayer, A.G. Cullis, H.C. Webber, N.G. Chew, J.M. Poate, and D.C. Jacobson, Phys. Rev. Lett. **50**, 896 (1983).

67. G.E. Jellison, J. Appl. Phys. **69**, 7627 (1991).

68. G.E. Jellison and D.H. Lowndes, Appl. Phys. Lett. **47**, 718 (1985).

69. H.K. Park, X. Xu, C.P. Grigoropoulos, N. Do, L. Klees, P.T. Leung, and A.C. Tam, Journal of Heat Transfer **115**, 178 (1993).

70. P.S. Peercy, J.Y. Tsao, S.R. Stiffler, and M.O. Thompson, Appl. Phys. Lett. **52**, 203 (1988).

71. R.F. Wood, D.H. Lowndes, and J. Narayan, Appl. Phys. Lett. **44**, 770 (1984).

72. G. Devaud and D. Turnbull, Appl. Phys. Lett. **46**, 844 (1985).

73. S.R. Stiffler, M.O. Thompson, and P.S. Peercy, Phys. Rev. Lett. **60**, 2519 (1988).

74. G. Devaud, Ph.D. Thesis, Harvard University (1986).

75. Private communication, Lambda Physik, Fort Lauderdale, FL.

76. D. Basting, Lambda Physik AG, 125 (2001).

77. I.-J. Chung, IDMC 2002 Proceedings, 415 (2002).

78. E. Fogarassy, S.d. Unamuno, P. Legagneux, F. Plais, D. Pribat, B. Godard, and M. Stehle, Thin Solid Films **337**, 143 (1999).

79. E. Fogarassy, S.d. Unamuno, B. Prevot, T. Harrer, and S. Maresch, Thin Solid Films **383**, 48 (2001).

80. E. Fogarassy, S. de Unamuno, P. Legagneux, F. Plais, D. Pribat, B. Godard, and M. Stehle, Thin Solid Films **337**, 143 (1999).

81. E. Fogarassy, S. de Unamuno, B. Prevot, P. Boher, M. Stehle, and D. Pribat, Appl. Phys. A **68**, 631 (1999).

82. D. Kim, Ph.D thesis, Columbia University (2002).

83. Y. Deng, Ph. D thesis, Columbia University (2010).

84. L. Csepregi, E.F. Kennedy, J.W. Mayer, and T.W. Sigmon, Journal of Applied Physics **49**, 3906 (1978).